A simple triangular multi-redox *pseudo*-[6]oxocarbon capable of accepting up to six electrons

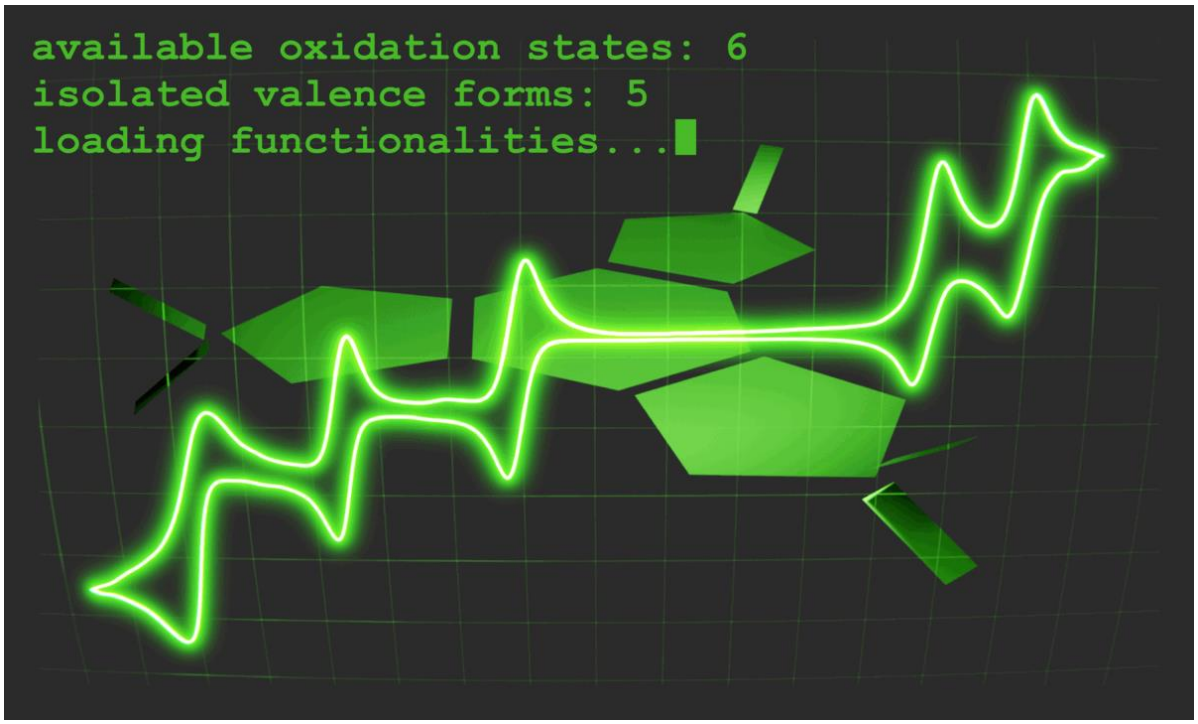

Paweł Pakulski,[a,*] Michał Magott,[a] Szymon Chorazy,[b] Marcin Sarewicz,[c] Monika Srebro-Hooper,[a] Dominika Tabor,[a] Łukasz Łapok,[a] Dariusz Szczepanik,[a] Selvan Demir[c] and Dawid Pinkowicz[a,*]

[a] Faculty of Chemistry, Jagiellonian University, Gronostajowa 2, 30-387 Kraków, Poland
[b] Department of Molecular Biophysics, Faculty of Biochemistry, Biophysics and Biotechnology, Jagiellonian University, Gronostajowa 7, 30-387 Kraków, Poland
[c] Department of Chemistry, Michigan State University, 578 South Shaw Lane, East Lansing, Michigan 48824, USA
* corresponding authors email addresses: dawid.pinkowicz@uj.edu.pl, p.pakulski@uj.edu.pl

Bigger picture

Energy efficient molecule-based materials are highly desired for the fabrication of green devices that can be easily scaled down to a subnanometer size with the ultimate limit being a single molecule. Suitable molecular candidates should show multifunctionality - a non-trivial coupling of properties leading to multiple input/output possibilities so they can act as a molecular sensor, switch, valve etc. Achieving multifunctional molecules is a challenging and yet high-gain task that would result

in single molecule devices operated by light, electric and/or magnetic fields or responsive to small signaling molecules. Herein, we report a simple derivative of the iconic [6]oxocarbon capable of accepting up to six electrons in five consecutive reduction steps. Successful isolation and crystallization of the reported compound in five-out-of-six possible oxidation states revealed a wide range of functionalities unexpected for such a simple molecular framework.

Abstract

Multi-electron redox chemistry is traditionally a domain of transition metals which are well-known to show multiple valence states with a vast variation of physical and chemical properties. Redox-active organic molecules, on the other hand, usually present only two valence states. Herein we demonstrate the design and preparation of a very simple organic molecule benzo[1,2-c:3,4-c':5,6-c'']tris([1,2,5]thiadiazole) 2,2,5,5,8,8-hexaoxide (**tripak**) that shows unprecedently rich redox chemistry and is capable of accepting up to six electrons in five consecutive reduction steps. **Tripak** is a derivative of the thermodynamically unstable [6]oxocarbon C_6O_6, where all C=O groups were used to form three dioxothiadiazole rings. It is the first representative of the new poly(dioxothiadiazole) family of compounds comprising three dioxothiadiazole groups fused together to form a simple rigid highly symmetrical skeleton with a single benzenoid ring in the middle. The electron withdrawing character of the dioxothiadiazole rings is responsible for the reversible multi-electron redox behavior which enabled its isolation and complete structural and physicochemical characterization in five-out-of-six oxidation states: 0, -1, -2, -3 and -4. Depending on the number of electrons, the **tripak** system represents different types of aromaticity (non-aromatic, Hückel or Baird) and redox-related multifunctionality: **tripak^{0}** shows record-strong anion-π binding of halides which is comparable with the energy of coordination bonds, **tripak^{1-}** and **tripak^{3-}** are two very different *S* = 1/2 radical states with **tripak^{1-}** exhibiting very long spin-spin relaxation time at room temperature placing it among the most promising molecular qubit candidates, **tripak^{2-}** is a blue dye with strong red fluorescence and finally **tripak^{4-}** is an open-shell singlet diradicaloid system with a singlet-triplet gap close to zero.

Introduction

Multiple oxidation states are typical for metals but quite rare for purely organic molecules. For instance, one of the most common metals - iron - has nine confirmed oxidation states, [1–9] while the 'best performing' redox-active organic molecules, [10] such as 2,3,5,6-tetra(2-pyridyl)pyrazine (tppz), [11] tetrapyridophenazine (tphz), [12] hexakis(guanidino)benzene [13] or bipyridine- and phenanthroline-based carbene architectures, [14] are characterized structurally in only up to four oxidation states. Despite the possibility of isolating various metal-based compounds in multitude of different oxidation states, true multivalency is rare among them because the redox reaction is usually associated with the exchange of the ligands resulting in a complete change of the chemical nature of the compound. There are, nevertheless, a few exceptions like the [Ru^{II}(2,6-bis(phenylazo)pyridine)$_3$]$(PF_6)_2$ [15] showing four accessible valence states, [$Cr(L_3)_3$] with six accessible valence states [16] or polyoxometalates (POMs) – multinuclear early transition metal systems such as $Li_6[P_2W_{18}O_{62}]$ [17] or $[NBu_4]_4[S_2W_{18}O_{62}]$ [18,19] (NBu_4^+ = tetrabutylammonium cation), which can accommodate multiple electrons in a series of multiple reversible reduction reactions (Figure 1A and 1B). These systems, however, are relatively large, e.g., the molar mass of the redox active species $[S_2W_{18}O_{62}]^{n-}$ exceeds 4000 g·mol^{-1}. Moreover, $[S_2W_{18}O_{62}]^{n-}$ could only be characterized structurally in two valence states with n = 4 and 5. [20] The situation for its Mo-analog is similar: only three valence states with n = 4, 5 and 6 [21–23] are reported according to the CCDC database. This marks the huge advantage of simple multivalent organic molecules: while their chemical connectivity remains

unchanged regardless of their oxidation state, the electronic structure, fine geometry, and physicochemical properties vary considerably, resulting in extraordinary color changes, magnetic properties switching and completely different reactivity depending on the number of accommodated electrons. Multi-redox organic molecules are perfect for the construction of fast molecule-sized junctions [24] or multistable multifunctional devices such as molecular memristors [15,25] switchable by electric potential. The more valence states such a molecule shows, the more versatile the possible molecular device would be. However, simple organic molecules that could accommodate more than four electrons are extremely rare and were never isolated in all accessible valence states.[26–28] We hereby fill this gap and report the first example of an organic molecule with six accessible valence states: benzo[1,2-c:3,4-c':5,6-c'']tris([1,2,5]thiadiazole) 2,2,5,5,8,8-hexaoxide (**tripak**) (Figure 1C and 1D).

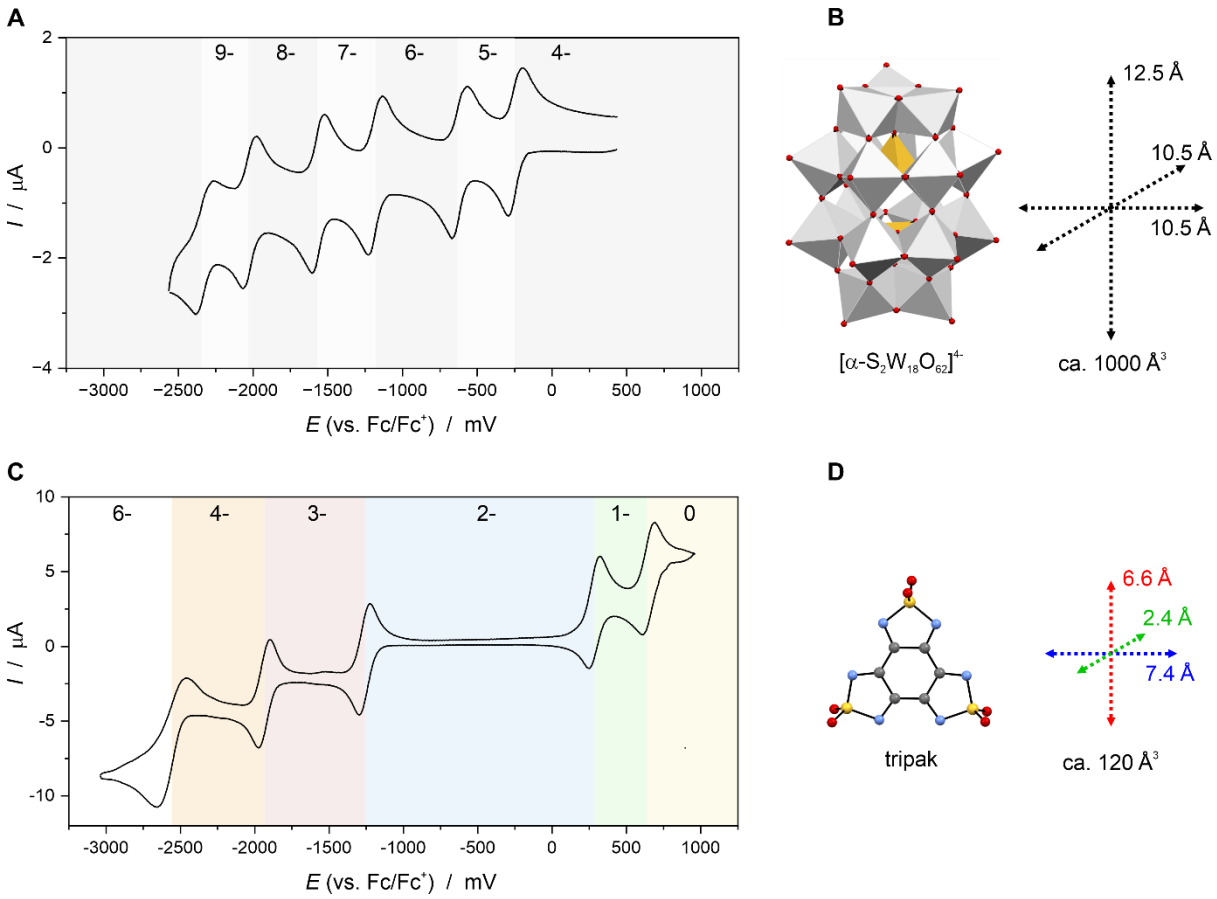

Fig. 1. Comparison of the high performance multi-redox polyoxometalate with the reported multi-redox organic molecule tripak. Cyclic voltammetry (CV) for $[\alpha\text{-}S_2W_{18}O_{62}]^{4-}$ POM (**A**, 5.0×10^{-4} M, 0.1 M NBu_4PF_6 in MeCN, 200 mV·s^{-1} sweep rate, glassy carbon electrode as reported in ref. [29]) and its crystal structure [30] with approximate dimensions and molecular volume of ca. 1000 Å^3 (**B**) compared to the CV for benzo[1,2-c:3,4-c':5,6-c'']tris([1,2,5]thiadiazole) 2,2,5,5,8,8-hexaoxide (**tripak**) (**C**, 0.1 M NBu_4PF_6 in THF, 25 mV·s^{-1} sweep, glassy carbon electrode) and its molecular structure (**D**) based on the single crystal X-ray diffraction (scXRD) with approximate volume of 120 Å^3. The numbers inside the CV plots in panels **A** and **C** indicate the charge of the electroactive species formed during the experiment.

The importance of the redox-active organic molecules is highlighted by many literature examples: methyl viologen, [31,32] tetrathiafulvalene (TTF) [33] or tetracyanoquinodimethane (TCNQ) [34] which exhibit only up to three valence states and yet, have attracted lots of attention over the years. The iconic $TTF^{+}TCNQ^{-}$ charge transfer salt was reported as the first organic conductor [35] which then exploded into a new field of organic conductors [36,37] and superconductors. [38,39] Moreover, organic multi-electron redox systems exhibit many attractive properties desirable in material sciences. Among others, they enable the design of environmentally friendly batteries [26,40] showing in some cases exceptionally large capacities [41] and grant access to multiswitching of physicochemical properties such as electric switching of light absorption/emission which found wide applications in electrochromic devices. [42]

Multivalent organic systems might also show radical or even diradical character with an enormous potential for the construction of molecule-based magnets. [43,44] Interest in organic radicals started as early as 1900's with the pioneer work of Gomberg related to the triphenylmethyl radical. [45] Since this discovery, the realm of intrinsically paramagnetic organic molecules has been expanded significantly [46–49] including the huge library of radical building blocks for the construction of functional molecular materials. [50] One of the most attractive concepts within the field of paramagnetic organic molecules are diradicals [51–53] or even multiradicals [54] which could drastically increase their usefulness for the construction of lightweight and/or ultra-hard single molecule magnets. [55–58]

In this paper we present the design, synthesis and characterization of a simple rigid organic molecule benzo[1,2-c:3,4-c':5,6-c'']tris([1,2,5]thiadiazole) 2,2,5,5,8,8-hexaoxide (**tripak**) which shows six accessible valence states as confirmed by electrochemical studies in solution. The compound was designed as the poly(dioxothiadiazole) derivative of the elusive [6]oxocarbon. Five-out-of-six accessible states: **tripak^{0}**, **tripak^{1-}**, **tripak^{2-}**, **tripak^{3-}** and **tripak^{4-}** were isolated and studied in the form of 12 crystalline salts with various cations (tetraphenylphosphonium PPh_4^+, tetrabutylammonium NBu_4^+ and/or tris(phenanthroline)iron(II) $[Fe^{II}(phen)_3]^{2+}$): **tripak^{0}**: $(NBu_4)_2Cl_2$tripak (**0a**), $(NBu_4)_2Br_2$tripak (**0b**), $(PPh_4)_2Cl_2$tripak (**0c**) and $(PPh_4)_2Br_2$tripak (**0d**); **tripak^{1-}**: $[Fe^{II}(phen)_3](PF_6)$tripak·1.6MeCN·0.4Et_2O (**1-a**) and $(NBu_4)_{1.5}$tripak·4THF (**1-b**); **tripak^{2-}**: $(NBu_4)_2$tripak (**2-a**), $(PPh_4)_2$tripak (**2-b**) and $(PPh_4)_2$tripak·2MeCN (**2-c**); **tripak^{3-}**: $(NBu_4)_3$tripak·THF (**3-a**) and $(PPh_4)_3$tripak (**3-b**); **tripak^{4-}**: $(NBu_4)_4$tripak·2THF (**4-a**). The compounds were fully characterized by single-crystal X-ray diffraction (scXRD) structural analysis, powder X-ray diffraction (PXRD), spectroscopy: NMR, EPR, IR and UV-vis, magnetic measurements and DFT calculations including the analysis of their electronic structure with particular highlight on. All these methods uneqivocally prove an unparalleled range of functionalities of this simple molecule. The diamagnetic **tripak^{0}** shows extreme affinity to halide anions and binds them via the strongest symmetric anion-π type interactions ever reported, **tripak^{-}** is an organic radical with very slow paramagnetic relaxation, **tripak^{2-}** shows high molar absorption in the UV-vis range and exhibits red fluorescence, **tripak^{3-}** is the second radical form and **tripak^{4-}** exhibits Baird aromaticity (according to DFT calculations) with very small triplet-singlet (S-T) energy gap which renders it a diradicaloid system. [59]

Results and Discussion

Design and synthesis of the tripak system in its native valence state

The **tripak** molecule was designed as a poly(dioxothiadiazole) derivative of the rhodizonate anion $[C_6O_6]^{2-}$ [60–62] and the analog of the phenanthro[9,10-c][1,2,5]thiadiazole 2,2-dioxide [63] (Figure 2A). It belongs to the archetypical family of [6]radialenes or *pseudo*-[6]oxocarbons. [64] **Tripak** synthesis was approached based on the existing synthetic strategies for the preparation of 1,1-dioxo-1,2,5-thiadiazoles [65] and diquinoxalino[2,3-*a*:2',3'-*c*]phenazine,[66] but required isolation in the form of a salt due to the dianionic character of its native form. Several known methods for the preparation of dioxothiadiazoles were tested to prepare **tripak** using dodecahydroxycyclohexane dihydrate and sulfamide as substrates (Figure 2): mechanochemical synthesis in the solid state, [67] liquid-assisted grinding, [68] solid-state melt,[69] microwave-assisted synthesis [70] and wet chemistry methods [71–74] (also including catalysts [75]).

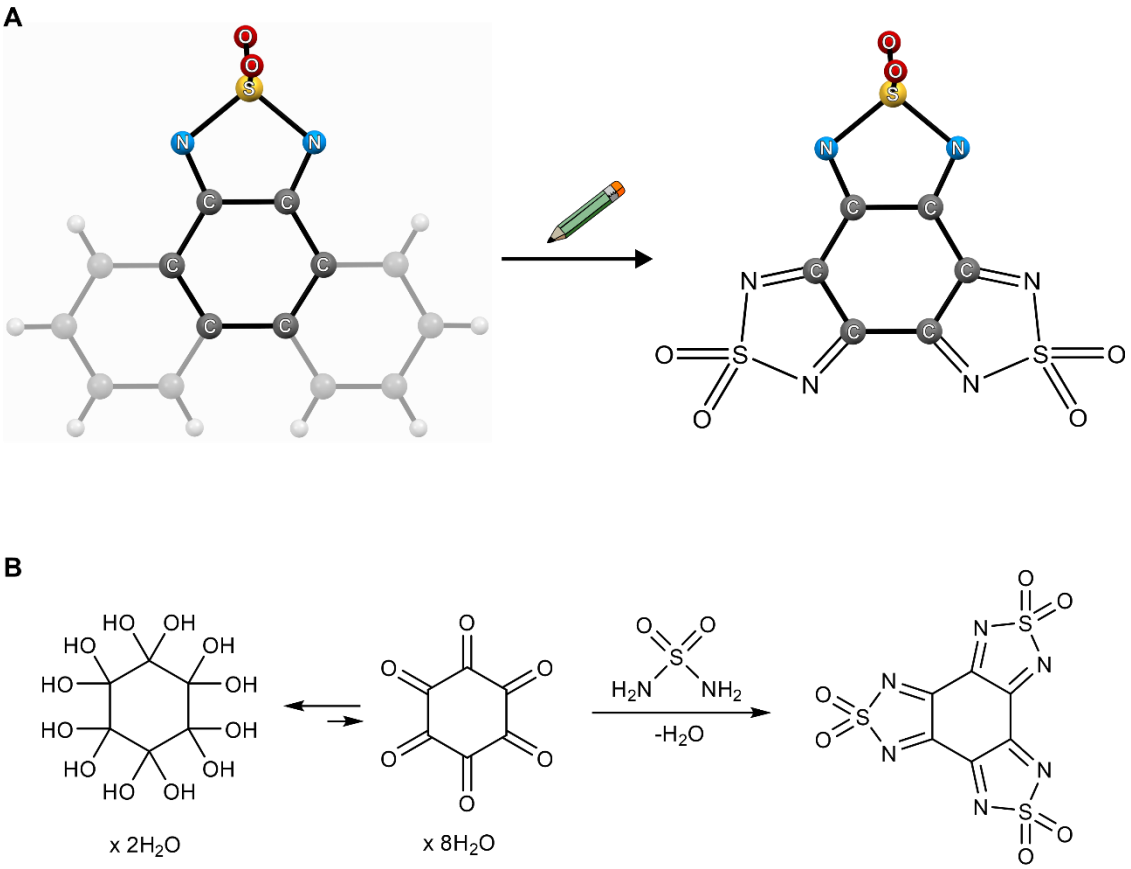

Fig. 2. Design concept and proposed synthetic route to tripak. The design concept is based on the replacement of the redox inactive phenyl rings in phenanthro[9,10-c][1,2,5]thiadiazole 2,2-dioxide by additional redox active dioxothiadiazole groups (**A**) leading to benzo[1,2-c:3,4-c':5,6-c'']tris([1,2,5]thiadiazole) 2,2,5,5,8,8-hexaoxide (**tripak**) – *pseudo*-[6]oxocarbon. Panel B depicts the proposed synthetic route to **tripak** via condensation of sulfamide and hexaketocyclohexane octahydrate.

One of the first attempts was typical for the preparation of dioxothiadiazoles: a reaction of sulfamide with a respective ketone refluxed in ethanol with or without the addition of strong mineral acid like HCl. Indeed, after several hours of reflux traces of products can be obtained in this manner, but it was clearly not a method meant for preparative quantities of the target compound. The issue was low solubility of the reactants and products in ethanol and the fact that dodecahydroxycyclohexane dihydrate is known to be thermally unstable and upon refluxing for a prolonged time at elevated temperature undergoes decarbonylation and other side reactions. [76,77]

For this reason, solid-state melt was also ruled out since a majority of the substrate was lost before the thermal activation barrier was reached. Microwaves were tested as an alternative heating method known to help in the case of compounds sensitive towards prolonged heating [78] but the results were not satisfactory either. Next, the mechanochemical approach was evaluated and surprisingly this proved to be almost equally effective as refluxing in ethanol without the problem of overheating the sensitive substrate. The drawbacks were laborious grinding in a mortar that needs to last for at least 20 minutes and the scale (ca. 50 mg) limiting the effectiveness of this method.

Laborious small-scale repetitions of the wet chemistry approach in various solvents enabled identification of the product as the dianion (the neutral molecule does not form in these reactions). This enabled the optimization of the reaction conditions that include the addition of a suitable countercation, ideally an inert one that would enhance the solubility of the dianionic product in organic solvents. Tetrabutylammonium and tetraphenylphosphonium were selected as they differ in solubility and crystallization properties but are both generally well soluble in most polar organic solvents and show good chemical stability. To further increase the yield and shorten the reaction time, an addition of sulfuric acid was necessary (ca. 1.8 eq. relative to ketone). It solves the problem of poor solubility of sulfamide in organic solvents as it most likely forms some reactive protonated species. [79] Finally, the reaction was carried out in acetonitrile instead of ethanol which in combination with the high load of organic salts and sulfuric acid allowed to increase the reflux temperature. To mitigate the possible thermal decomposition of the hexaketocyclohexane octahydrate precursor, it is added in portions to a refluxing mixture of the reactants to support fast conversion to the desired products with minimal losses. Multigram scale reactions were successfully performed in this manner with >50% overall yield based on the 'ketone' precursor. This is satisfactory given the fact that the actual reaction leading to the dianionic products must involve a redox process between the neutral species (being very reactive and strong oxidants) formed in the original condensation and other components of the reaction mixture like Br^- anions (from NBu_4Br/PPh_4Br), water or even the ketone source being unstable and prone to decomposition.

Electrochemistry and redox reactivity of the tripak system

The striking feature of the studied system is its ability to accommodate six electrons within its simple molecular framework comprising only 21 *p*-block atoms. This is revealed by cyclic voltammetry (Figure 1C and Figure 3) and confirmed by the crystallization of **tripak** in five-out-of-six accessible oxidation states: 0, -1, -2, -3 and -4 followed by the extensive physicochemical characterization of the resulting compounds. Cyclic voltammetry recorded in the -3000 to 1000 mV range vs Fc/Fc^+ in THF (Figure 3) shows five well-defined reversible electron transfer steps four of which are one-electron and one is a two-electron process. The reversible potentials of **tripak^{2-}** in various solvents vs Fc/Fc^+ for accessible redox couples: tripak$^{0/1-}$, tripak$^{1-/2-}$, tripak$^{2-/3-}$, tripak$^{3-/4}$, tripak$^{4-/6-}$ are summarized in Table 1 and depicted in Figure 3. As evidenced, **tripak** can be considered a strong or even very strong oxidant if isolated as a neutral molecule **tripak^0** or strong reductant when isolated in the form of a tetraanionic or hexaanionic species as compared to known oxidants/reductants commonly used in organometallic chemistry. [80]

Table 1. Details of the cyclic voltammetry measurements. Reduction (E_{red}), oxidation (E_{ox}) and half potentials ($E_{1/2}$ = (E_{red} + E_{ox})/2) in (mV) vs. Fc/Fc^+ for $(NBu_4)_2$tripak recorded in THF, MeCN, DCM and DMF. Data collected on glassy carbon electrode with 0.1 M $(NBu_4)PF_6$ as the supporting electrolyte with the scan rate of 25 $mV{\cdot}s^{-1}$. Color coding for E_{red} and E_{ox} corresponds to that used in Figures 1 and 3. Values of E_{red}, E_{ox} and $E_{1/2}$ are provided with ±5 mV accuracy.

Solvent	$E_{1/2}^{6-/4-}$		$E_{1/2}^{4-/3-}$		$E_{1/2}^{3-/2-}$		$E_{1/2}^{2-/1-}$		$E_{1/2}^{1-/0}$	
	E_{red}	E_{ox}	E_{red}	E_{ox}	E_{red}	E_{ox}	E_{red}	E_{ox}	E_{red}	E_{ox}
THF	**-2559**		**-1935**		**-1260**		**+286**		**+649**	
	-2655	-2462	-1972	-1897	-1295	-1225	+248	+323	+608	+689
MeCN			**-1704**		**-1100**		**+451**		**+734**	
			-1733	-1675	-1126	-1073	+425	+478	+705	+763
DCM			**-1823**		**-1153**		**+474**		**+717**	
			-1875	-1770	-1198	-1108	+433	+514	+672	762
DMF	**-2836**		**-1959**		**-1215**		**+321**		**+489**	
	-2990	-2682	-1995	-1923	-1244	-1187	+292	+349	+458	520

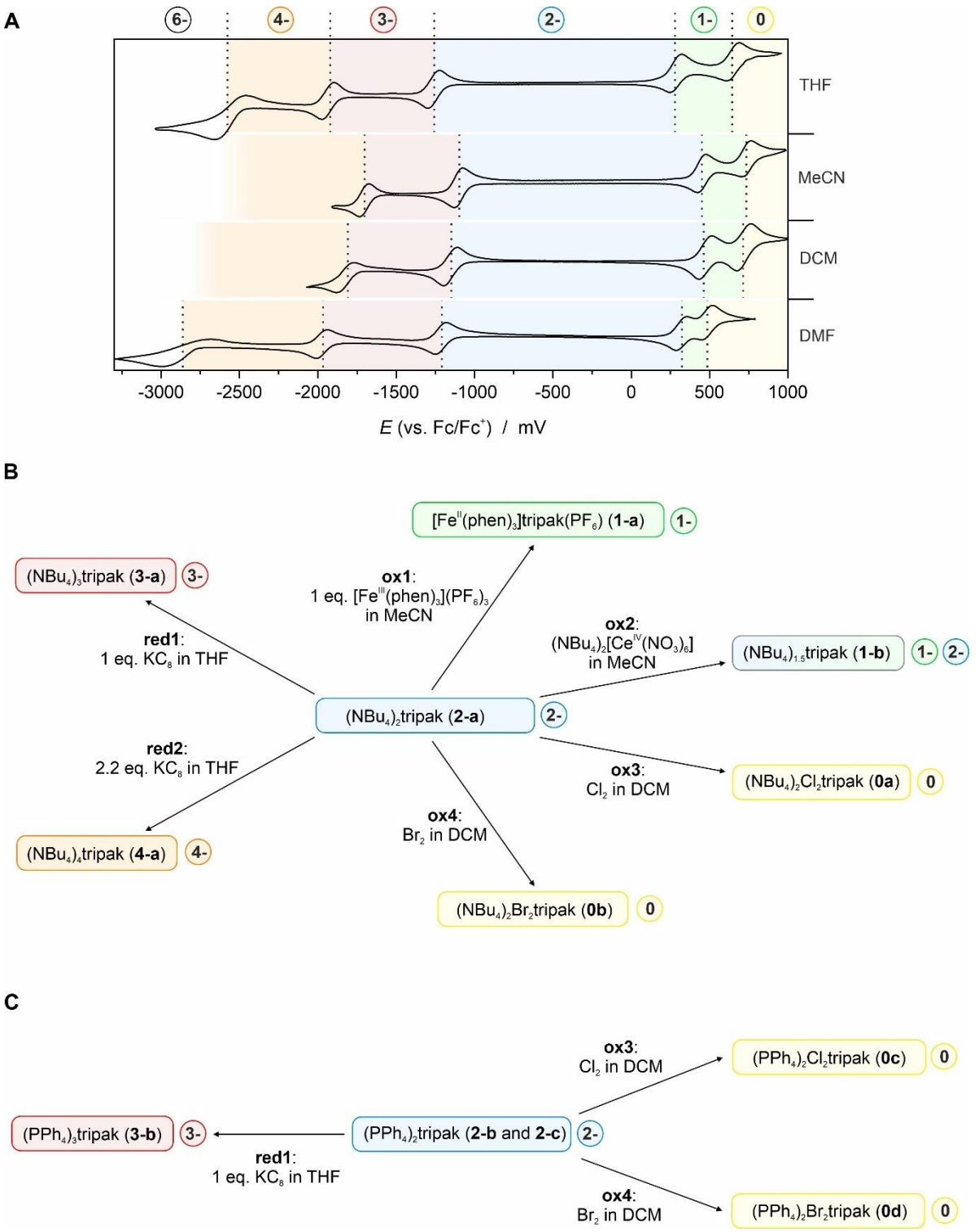

Fig. 3. Cyclic voltammetry of tripak in various solvents and chemical reduction/oxidation reaction pathways leading to relevant tripak products. Comparison of the cyclic voltammetry (CV) for **tripak** recorded using glassy carbon electrode and 0.1 M NBu_4PF_6 electrolyte with 25 $mV \cdot s^{-1}$ sweep (**A**): in THF, MeCN, DCM and DMF. Reaction pathways towards all accessible valence states of **tripak** starting from the tetrabutylammonium salt of **tripak**$^{2-}$ dianion (**B**) and tetraphenylphosphonium salts of **tripak**$^{2-}$ dianion (**C**). Numbers in circles indicate the charge of the tripak and the colors correspond to the background in the cyclic voltammograms (**A**).

Based on the electrochemical studies, suitable reductants and oxidants were selected to perform chemical redox reactions starting from the native form of **tripak^{2-}** to isolate this molecule in all accessible valence states. Figures 3B and 3C summarize the performed reaction routes and twelve isolated compounds. Oxidation to neutral species was best performed using chlorine Cl_2 (ca. +0.7 V vs Fc/Fc^+) and bromine Br_2 (ca. +0.4 V vs Fc/Fc^+) while oxidation by iodine I_2 (+0.1 V vs Fc/Fc^+) proved to be unsuccessful. The formal potentials of these halogens vs Fc/Fc^+ in MeCN were calculated based on the available literature. [80–84]

Oxidation of $(NBu_4)_2$tripak to its neutral form was also successfully attempted using $NOBF_4$ (+0.87 V vs Fc/Fc^+ in MeCN). However, the low yield and a large amount of unidentified byproducts rendered this oxidant unsuitable for large scale preparations. [85] Oxidation of both native forms $(NBu_4)_2$tripak (**2-a**) and $(PPh_4)_2$tripak (**2-b**) led to the successful isolation of $(NBu_4)_2Cl_2$tripak (**0a**) and $(PPh_4)_2Cl_2$tripak (**0c**) when Cl_2 was used or $(NBu_4)_2Br_2$tripak (**0b**) and $(PPh_4)_2Br_2$tripak (**0d**) in the case of oxidation with Br_2. In these oxidation products, **tripak^0** molecules co-crystallize with NBu_4Cl, PPh_4Cl, NBu_4Br and PPh_4Br, respectively, resulting in a very peculiar sandwich-type geometry X···tripak^0···X (X = Cl^- or Br^-). This type of chemical assembly arises from record-strong anion-π interactions, [86–88] which will be discussed in the following sections.

Oxidation to monoanions is particularly challenging as the electrochemical stability window for this valence state calculated as the difference between $E_{red}^{1-/0}$ and $E_{ox}^{2-/1-}$ (see Table 1) is narrow: 285 mV in THF, 227 mV in MeCN, 158 mV in DCM and only 109 mV in DMF. A suitable oxidant needs to meet several requirements: 1e$^-$ oxidation must take place in a narrow electrochemical window, the oxidant must be soluble either in THF or MeCN and should facilitate the removal of the redundant organic cations. Ce(IV) in the form of the tetrabutylammonium salt of $[Ce^{IV}(NO_3)_6]^{2-}$ anion: $(NBu_4)_2[Ce^{IV}(NO_3)_6]$ (CTAN) was found to be suitable (Ce^{IV}/Ce^{III} couple $E_{1/2}$ = +0.610 V vs Fc/Fc^+ in MeCN, Figure S1 in the SI). However, the corresponding oxidation of $(NBu_4)_2$tripak (**2-a**) resulted in the formation of a mixed-valence salt, in which each tripak anion was accompanied by 1.5 NBu_4^+ cations: $(NBu_4)_{1.5}$tripak·4THF (**1-b**) that leads to the conclusion that it comprises both **tripak^{1-}** and **tripak^{2-}** in a 1:1 ratio. Therefore, another oxidant was used to prepare **tripak^{1-}**: $[Fe^{III}(phen)_3](PF_6)_3$ [89] with formal potential of the Fe^{III}/Fe^{II} couple $E_{1/2}$ = +0.696 V vs Fc/Fc^+ in MeCN, Figure S2 in the SI). Oxidation of $(NBu_4)_2$tripak (**2-a**) in MeCN with $[Fe^{III}(phen)_3](PF_6)_3$ proceeds smoothly resulting in the formation of **tripak^{1-}** salt that incorporates $[Fe^{II}(phen)_3]^{2+}$ as the countercation and PF_6^- as an additional counteranion: $[Fe^{II}(phen)_3](PF_6)$tripak·1.6MeCN·0.4Et_2O (**1-a**).

Chemical reduction of **tripak^{2-}** to the trianionic species **tripak^{3-}** was achieved using KC_8 in anhydrous MeCN or THF and in the presence of excess NBu_4^+ cations to avoid the formation of mixed potassium-tetrabutylammonium systems. Addition of a slight excess of KC_8 to the blue solution of $(NBu_4)_2$tripak (**2-a**) results in a fast color change to brown due to the formation of $(NBu_4)_3$tripak·THF (**3-a**). Similarly, reduction of $(PPh_4)_2$tripak (**2-b**) with stoichiometric amount of KC_8 leads to the tetraphenylphosphonium salt of **tripak^{3-}**: $(PPh_4)_3$tripak (**3-b**). If excess of KC_8 is used in benzene or toluene (slightly more than 2 eq. relative to **tripak^{2-}**), the color of the solution changes to orange and isolation of the tetraanion **tripak^{4-}** in the form of $(NBu_4)_4$tripak·2THF salt (**4-a**) is possible.

Crystal structures and electronic properties of the tripak system in various valence states

Tripak was crystallized in five different valence states represented by twelve compounds (Figure 3B and 3C) which were all characterized by means of scXRD structural analysis at 100 K (see the SI: Tables S1-S12 for selected crystallographic data and Panels S1-S12 for the asymmetric units, packing diagrams and bond length lists). The purity/identity of the compounds was confirmed by

powder X-ray diffraction (PXRD; Figures S3-S14 in the SI) which were compared against the respective simulated patterns from scXRD measurements repeated at 270 K for each crystal. The corresponding *cif* files containing the *fcf* tables are deposited within the Cambridge Structural Database (CSD) of the Cambridge Crystallographic Data Centre CCDC 2238791-2238802 (see Tables S1-S12 in the SI for XRD data collection and refinement details). The discussion of all reported crystal structures will be focused on the geometry of the **tripak** moiety in five different oxidation states. According to its design, **tripak** consists entirely of three 1,2,5-thiadiazole 1,1-dioxide units fused together via the central C_6 ring so that all atoms except oxygens lay on the same plane. The three sulfur atoms occupy the vertices of a nearly perfect equilateral triangle while the oxygen atoms of the $>SO_2$ groups point above and below its plane. The **tripak** system retains approximate D_{3h} geometry in all valence states (Figure 1D and Figure 4). The respective bond lengths within the **tripak** backbone change depending on the number of accommodated electrons: on average C-C and S-N bonds shrink while C-N and S-O bonds expand upon electrochemical/chemical reduction (see Figure 4 and Table 2). Interestingly, the total relative change of some of the bond lengths like C-C and C=N are as large as those in some spin crossover complexes based on iron(III) [90] potentially relevant as molecular photoswitching devices. Detailed lists of all bond lengths for each crystal structure of **tripak** can be found in Panels S1-S12 in the SI. These lists are accompanied by detailed plots (Figures S15-S19 in the SI) showing the distribution of individual experimental and calculated bond lengths for each valence state. See SI for a description of computational details, and Tables S13-S22 in the SI for the calculated geometries of **tripak** in various valence states, assuming spin-singlet and spin-triplet electronic configurations, and the presence/absence of halides, where applicable.

Table 2. Summary of the experimental mean bond lengths and corresponding mean standard deviation in the **tripak** molecular scaffold depending on its valence state and the respective bond length changes. Note that the data for the **tripak** structure in $(NBu_4)_{1.5}$tripak·4THF **1-b** were excluded from the calculation of average values due to the mixed-valence characte of the compound.

	C-C_{ring}	C-C_{inter}	C=N	S-N	S=O
tripak^{0}	1.505(4)	1.474(5)	1.278(4)	1.692(5)	1.423(3)
tripak^{1-}	1.489(3)	1.451(7)	1.290(3)	1.686(5)	1.425(3)
tripak^{2-}	1.471(5)	1.440(5)	1.310(8)	1.673(7)	1.434(4)
tripak^{3-}	1.458(12)	1.426(11)	1.333(12)	1.651(12)	1.441(5)
tripak^{4-}	1.455(38)	1.401(38)	1.360(32)	1.630(29)	1.451(15)
Total absolute change [Å]	-0.050	-0.073	+0.082	-0.062	+0.028
Total relative change [%]	-3.3	-5.0	+6.4	-3.7	+2.0

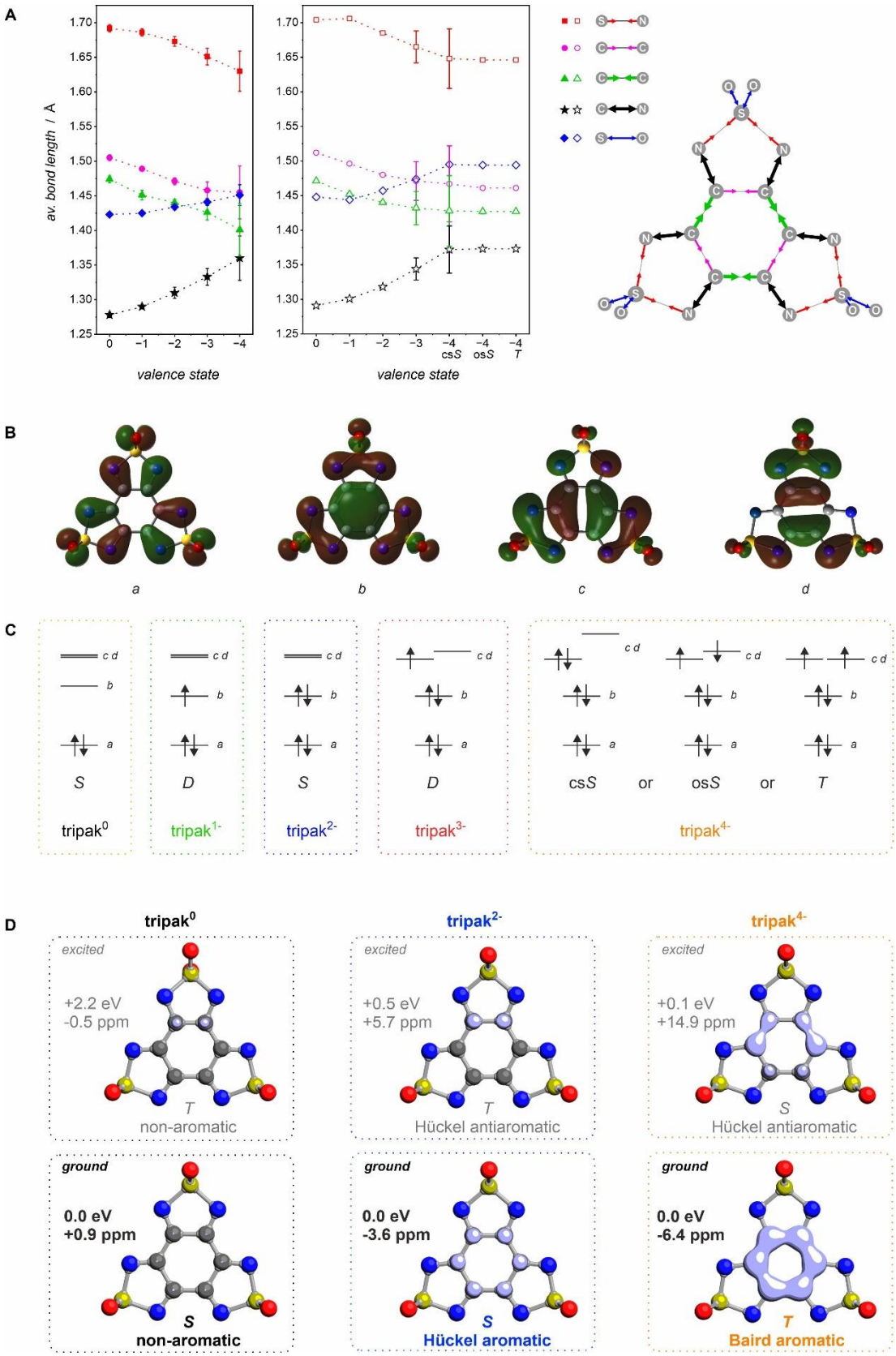

Fig. 4. Molecular geometry changes (A), frontier orbitals (B), electronic configurations (C) and aromaticity variations (D) upon reduction/oxidation of tripak. Plots showing the mean bond length variations (**A**) within the **tripak** molecular scaffold: experimental (left) and calculated (right) together with the graphical representation of its “redox breathing”. For more details see "Bond length analysis"

section in the SI, Figures S15-S19. Isosurfaces of the frontier orbitals of **tripak** (**B**) as calculated for **tripak**$^{2-}$ with the corresponding electronic configurations of all **tripak**$^{q-}$ states rationalizing the observed bond length variations (for details see text; q = 0, 1, 2, 3, 4, including closed-shell singlet cs*S*, open-shell singlet os*S* and triplet *T* configurations for tripak^{4-}) (**C**). Calculated electron density of delocalized bonds visualized for selected **tripak**$^{q-}$ (q = 0, 2, 4) at their equilibrium geometries (**D**) in the ground triplet state (bottom) and the closed-shell singlet configuration (top): black/gray numbers denote the energy of the state (eV) and the NICS(1) values (ppm).

The average change in the bond lengths observed experimentally (Figure 4A left) are perfectly reproduced by DFT geometry optimizations (see Figure 4A right and Tables S13-S22 in the SI for the optimized structures) and can be rationalized by looking at the shape of the frontier orbitals of the **tripak** system which are populated when going from **tripak**^{0} to **tripak**$^{4-}$ thus providing a handbook example of "quantum chemistry in action". The LUMO orbital of **tripak**^{0} (orbital *b* in Figure 4B) is delocalized over the whole molecule and shows clear bonding character within the C_6 ring and antibonding character for all C-N bonds. Hence, the addition of electrons to this orbital results in the pronounced shortening of the C-C bonds and elongation of the C-N bonds upon reduction to **tripak**$^{1-}$ and **tripak**$^{2-}$. As a result, the C-N bonds lose their double bond character while the C-C bonds are no longer single bonds but become stronger and gain benzene-like character when **tripak**^{0} is reduced to **tripak**$^{2-}$. The next two available orbitals (orbitals *c* and *d* in Figure 4B) also demonstrate bonding character for C-C and antibonding for C-N, which indeed explains further shortening of C-C and elongation of C-N bonds when two more electrons are added to **tripak**$^{2-}$. Interestingly, DFT optimized structures of **tripak**^{0} and **tripak**$^{2-}$ show clear degeneracy of the orbitals *c* and *d*, which suggests that **tripak**$^{4-}$ might be a diradical S = 1 system with two unpaired electrons occupying *c* and *d* orbitals according to the Hund's rule. The results of the respective geometry optimizations for **tripak**$^{4-}$ confirm that the spin-triplet configuration is lower in energy by 2.3 kcal·mol^{-1} (ca. 800 cm^{-1}) than the spin-singlet S = 0 configuration. However, the spin-singlet configuration corresponds to the unrestricted broken-symmetry solution, in which one spin-up unpaired electron and one spin-down unpaired electron are localized in different regions of space following distributions of electron density in the orbitals *c* and *d*; note that the closed-shell spin-singlet electronic configuration of **tripak**$^{4-}$, although easily computed, revealed an external instability of its wavefunction.

The nearly perfect triangular geometry of the calculated optimized **tripak**$^{4-}$ does not match, however, the one observed experimentally (scXRD structural model for $(NBu_4)_4$tripak·2THF **4-a**). The experimental structure shows a very clear distortion from the ideal D_{3h} towards C_{2v} symmetry. This is demonstrated as a significant deviation of particular bonds from the mean values (see Table 2, Figure 4A and Figures S15-S19 in the SI) in the structure of **tripak**$^{4-}$. Such distortion might lift the degeneracy of the *c* and *d* orbitals depicted in Figure 4B, leading to a singlet electronic configuration of **tripak**$^{4-}$ in compound **4-a**. Single point energy calculations for the experimental **tripak**$^{4-}$ structure extracted from **4-a** revealed that the open-shell broken-symmetry spin-singlet solution is ca. 2.9 kcal·mol^{-1} (ca. 1000 cm^{-1}) lower in energy than the pure triplet state, indicating that in its ground state **tripak**$^{4-}$ might be a mixture of singlet and triplet states. This mixed character of the **tripak**$^{4-}$ ground state will be demonstrated and discussed in the following sections describing the magnetic properties of the **tripak** system and a section focusing on **tripak**$^{4-}$ itself.

Evidenced by scXRD structural analysis and DFT calculations, **tripak** is a highly symmetric system with extensive delocalization of electrons over its whole backbone. In the case of 1-, 2-, 3- and 4- charged species, some of the electrons are also delocalized over the central benzenoid C_6 ring and

in the case of 2- and 4- fulfill the requirements for Hückel's (4n + 2) and Baird's (4n) aromaticity. Detailed DFT computations show that **tripak^{0}** is completely non-aromatic, **tripak^{2-}** is Hückel aromatic while **tripak^{4-}** is Baird aromatic in the triplet state and antiaromatic in the closed-shell spin-singlet configuration. In other words, **tripak** system provides a complete overview of all types of aromaticity within a single molecular framework.

To assess the aromatic character of the benzenoid ring in **tripak** at different valence states with even number of electrons the nucleus-independent chemical shift (NICS) at 1Å above the centroid of the ring was calculated. Noticeable negative and positive NICS values identify potentially aromatic and antiaromatic rings, respectively. [91] To confirm that the magnetic shielding probed by NICS is not affected by local currents from the surrounding lone pairs but is associated with cyclic delocalization of electrons, and hence aromaticity, the electron density of delocalized bonds (EDDB) was used. [92] NICS(1) values and EDDB isosufrace contours together with the relative singlet-triplet energy gaps are presented in Figure 4D.

In the neutral **tripak^{0}** there is no π-electron density associated with the C-C bonding in the central C_6 ring, which is well reflected by NICS(1) approaching zero and EDDB showing no cyclically delocalized electrons. Neutral **tripak^{0}** is therefore clearly not π-aromatic. In **tripak^{2-}** on the other hand, NICS(1) assumes negative value and EDDB shows uniform distribution of cyclically delocalized π-electrons in the benzenoid ring. This suggests weak π-aromaticity (Hückel aromaticity) in the ground-state closed-shell (singlet) configuration. Adding another two electrons into the system brings diradicaloid character of **tripak^{4-}**, as the singlet-triplet energy gap is now close to zero. The spin-triplet configuration features Baird π-aromaticity, as revealed by NICS(1) and EDDB (i.e., about 49% and 42% of the total spin density is attributed to carbon and nitrogen atoms, respectively). The closed-shell spin-singlet configuration, on the other hand, features Hückel antiaromaticity.

Physicochemical properties associated with various valence states of tripak

As elaborted above, the addition/removal of electrons to **tripak** system results in colossal changes in its electronic structure translating directly into significant color changes from yellow (**tripak^{0}**) through reddish or blue (**tripak^{1-}**) dark blue with red fluorescence (**tripak^{2-}**), greenish-brown (**tripak^{3-}**), to dark orange (**tripak^{4-}**) as evidenced by UV-vis spectroscopy (Figure 5A-E). Significant systematic changes in the IR (Figure 5F-J) and some changes in the NMR spectra (Figure 6) are also observed. For instance, the most intense IR band corresponding to the symmetrical stretching vibration of the S=O groups is successively red-shifted with each additional electron from 1178 through 1162, 1140, 1098 to 1073 cm^{-1} for **tripak^{0}** to **tripak $^{4-}$**, respectively, and these changes are consistent with the DFT calculations (bars in Figures 5F-J). Such a systematic shift could not be observed for other bands due to their overlap with tetrabutylammonium cations. The tripak system itself is ^{1}H NMR silent and only a single signal in the 140-160 ppm range is present in the ^{13}C NMR spectra for **tripak^{2-}** and **tripak^{0}** (Figure 6A). The native form **tripak^{2-}** (compound **2-a**) shows a single peak at 149.71 ppm (CD_3CN) regardless of the countercation. Upon oxidation, the peak shifts to either 152.97 or 153.56 ppm for $(NBu_4)_2Cl_2$tripak (**0a**) and $(NBu_4)_2Br_2$tripak (**0b**), respectively. This is most probably due to the typical de-shielding effect associated with the removal of two electrons from the HOMO orbital delocalized over the C_6 ring of **tripak^{2-}** upon oxidation to **tripak^{0}**. The slightly different trends for the bromide and chloride adducts are due to the differences between the electronic properties of Cl^- and Br^-: number of electrons, ionic radii, electron density distribution and electronegativity. Other valence states of the tripak system: **tripak^{1-}**, **tripak^{3-}** and **tripak^{4-}** are both ^{1}H and ^{13}C NMR silent due to their radical/diradicaloid character causing much faster relaxation and

broadening of the ^{13}C signals. Nevertheless, the ^{1}H NMR signals of the tetrabutylammonium cations display interesting shifts, which depend (although not systematically) on the valence state of **tripak** (Figure 6B). More importantly, however, a substantial broadening of these signals is observed for both radical states **tripak^{1-}** and **tripak^{3-}** as well as for the diradicaloid **tripak^{4-}** suggesting that the triplet state of the **tripak^{4-}** might be significantly populated at room temperature and as such its unpaired electrons might be involved in some interactions with the hydrogen and carbon atoms of the tetrabutylammonium cations leading to the broadening of their respective NMR signals. This hypothesis regarding the diradicaloid character of **tripak^{4-}** is consistent with the absence of the carbon signal in the ^{13}C NMR spectrum.

Other physical and chemical properties of the **tripak** system are also strongly affected by the redox processes while its molecular scaffold remains intact (Figure 4). The most unique features associated with each valence state will be discussed in the following sections starting from the neutral **tripak^{0}** which shows the ability to form the strongest ever reported anion-π interactions with halides. Afterwards the electronic and magnetic properties of the open-shell states **tripak^{1-}** and **tripak^{3-}** will be presented along with the peculiar case of **tripak^{4-}** which shows a very small triplet-singlet gap and is an example of a diradicaloid system with non-negligible population of the S = 1 spin state at room temperature. The discussion will be concluded by demonstrating the properties of the native valence state **tripak^{2-}** showing large molar absorption coefficient in the UV-vis range typical for organic dyes accompanied by relatively strong red luminescence.

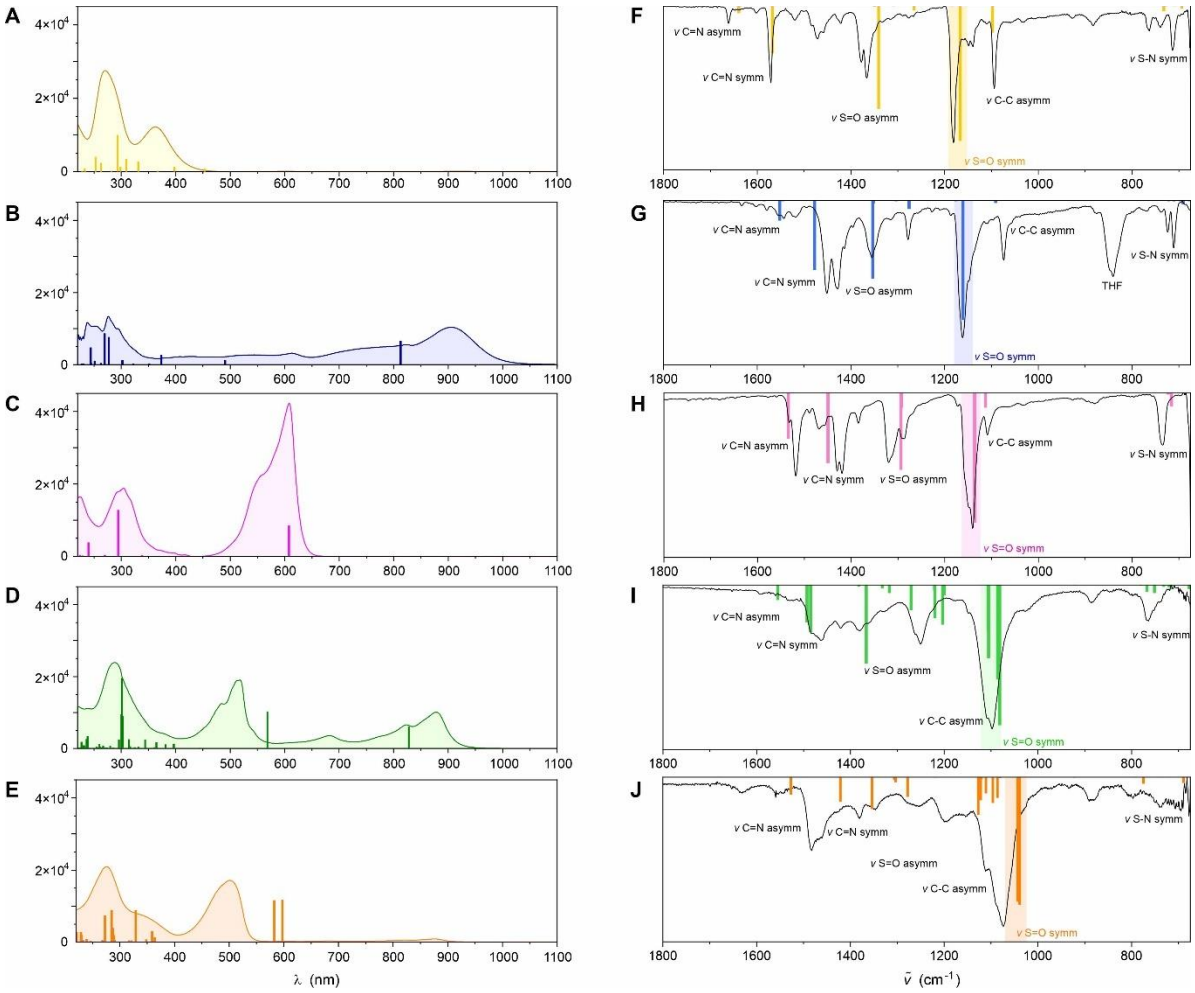

Fig. 5. UV-vis and IR spectra of the tripak redox system. Plots showing the UV-vis spectra recorded in THF at room temperature (**A**-**E**) and IR spectra recorded for crushed crystals (**F**-**J**) for **tripak^{0}** (**A** and **F**; compound **0a**), **tripak^{1-}** (**B** and **G**; compound **1-b**), **tripak^{2-}** (**C** and **H**; compound **2-a**), **tripak^{3-}** (**D** and **I**; compound **3-a**) and **tripak^{4-}** (**E** and **J**; compound **4-a**). Bars indicate calculated UV-vis excitation energies (**A**-**E**) or vibration modes frequencies (**F**-**J**) scaled by factor of 1.03 and IR intensities (bars in **E** and **J** represent DFT calculations results for an open-shell singlet configuration of **tripak^{4-}**). The S=O stretching vibration shows systematic blue shift (color highlights in **F**-**J**) when going from the neutral **tripak^{0}** towards the anionic **tripak^{4-}** which is consistent with the increase in the S=O bond length presented in Figure 4 and Figure S19 in the SI. Calculated UV-vis and IR spectra of **tripak^{0}** (A and F) as found in compounds **0a** and **0b**.

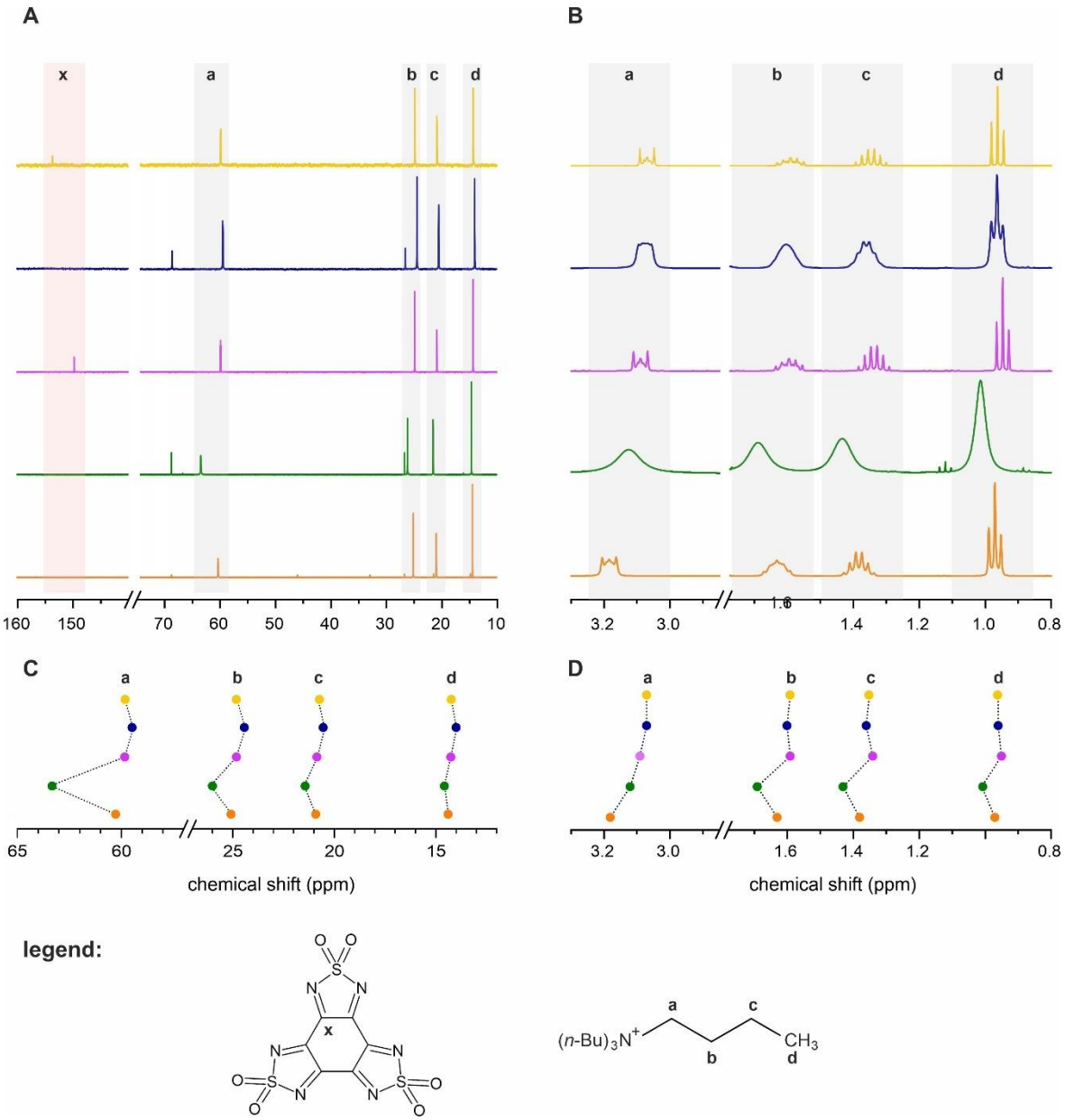

Fig. 6. ^{13}C NMR and ^{1}H NMR spectra of the tripak redox system. ^{13}C NMR (**A**) and ^{1}H NMR (**B**) spectra recorded in CD_3CN and the shifts of the corresponding NMR multiplets (**C** and **D**) for different valence states of **tripak** with tetrabutylammonium countercations: **tripak^{0}** in compound **0a** (yellow), **tripak^{1-}**

in compound **1-b** (navy blue), **tripak^{2-}** in compound **2-a** (magenta), **tripak^{3-}** in compound **3-a** (green) and **tripak^{4-}** in compound **4-a** (orange). The legend shows the NMR signal assignment.

Properties of tripak^{0}

Oxidation of **tripak^{2-}** using halogens Cl_2 or Br_2 leads to the formation of dianionic **X···tripak^{0}···X** assemblies (X = Cl^- or Br^-): $(NBu_4)_2Cl_2$tripak (**0a**), $(NBu_4)_2Br_2$tripak (**0b**), $(PPh_4)_2Cl_2$tripak (**0c**) and $(PPh_4)_2Br_2$tripak (**0d**) in which two halide anions are strongly bound to the neutral **tripak^{0}** and are almost perfectly centered above and below the plane of the molecule (Figure 7A). Such a molecular arrangement where two halides are placed so close to the π-deficient C_6 ring is unusual in the field of anion-π bonds - usually there is only one halide interacting with a given π-deficient ring and the typical distance is larger than 3.0 Å. The electroneutrality of the crystal structures in this series of compounds is ensured by the presence of two tetrabutylammonium or tetraphenylphosphonium cations per **dihalide-tripak^{0}** assembly. The distances between the halide anions and the center of the tripak molecule in all four compounds are extremely short. The average value for the chloride adduct is 2.419(14) Å based on the structures of $(NBu_4)_2Cl_2$tripak (**0a**) and $(PPh_4)_2Cl_2$tripak (**0c**) while for the bromide adduct it amounts to 2.563(8) Å based on the structures of $(NBu_4)_2Br_2$tripak (**0b**) and $(PPh_4)_2Br_2$tripak (**0d**). It is thus slightly shorter for chloride contacts than for bromide ones. Noteworthy, these distances do not depend on the type of the cation used for crystallization suggesting that the energy of the interaction between **tripak^{0}** and the two anions is the dominant factor responsible for the formation of these anion-π assemblies. The crystal packing seems to play a negligible role in this case. This is further supported by DFT geometry optimizations for the isolated **X···tripak^{0}···X** adducts (Tables S21 and S22 in the SI) which led to the following calculated distances between the halide anions and the centroid of the C_6 ring of **tripak^{0}**: 2.436 Å for X = Cl^- and 2.625 Å for X = Br^- – very similar to those observed experimentally.

It should be highlighted that the shortest Cl-C distance within the tripak···Cl^- structural motif in **0a** and **0c** of 2.790(3) Å is visibly shorter than the corresponding one between *p*-benzoquinone derivative DDQ and Cl^- (2.832(5) Å) reported in ref. [93], and thus - to the best of our knowledge - tripak···Cl^- structural motif represents the shortest chloride-π-acceptor contact to date. Similarly, the tripak···Br^- distances in **0b** and **0d** are significantly shorter than the one between hexaazatriphenylenehexacarbonitrile $HAT(CN)_6$ and Br^- of 3.26 Å in the corresponding motif found in the crystal structure reported in ref. [94] In order to provide a more quantitative description of the interactions between tripak and halide(s) in the reported assemblies, we have performed quantum-chemical calculations confirming that they are extremely strong, and in a way, resemble coordination bonds: they are highly directional, as strong as typical coordination bonds [95] and in this particular case, they are formed via the oxidative addition reaction of halogens to the divalent **tripak^{2-}** - similar to the oxidative addition of halogens to square planar complexes of platinum(II) (Figure 7B). [96]

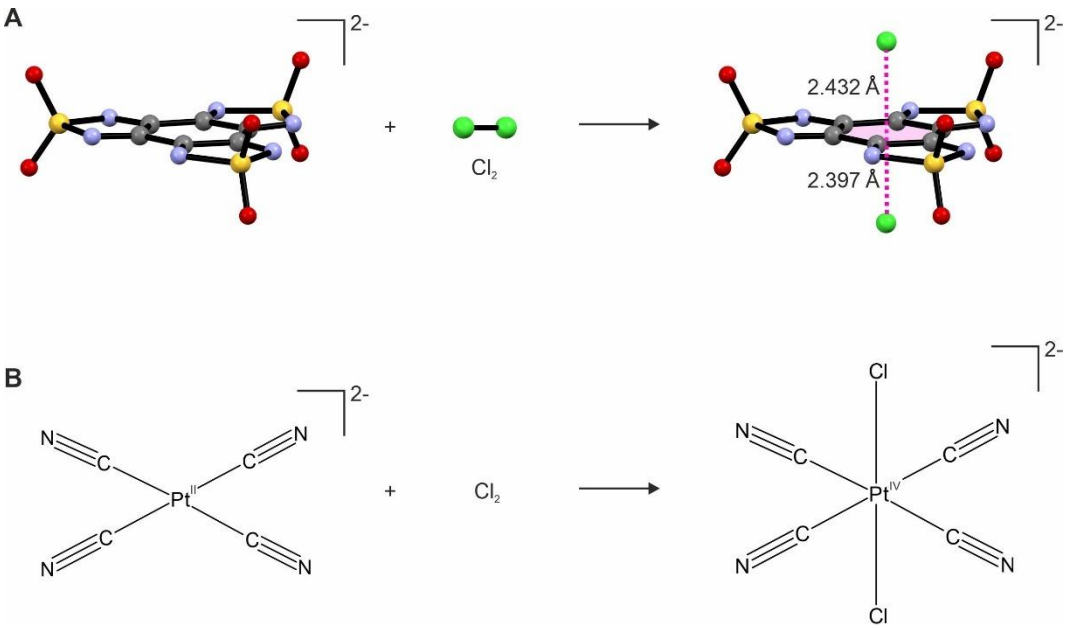

Fig. 7. Oxidative addition of chlorine to tripak^{2-} similar to the reactivity of tetracyanoplatinate(II). **Tripak^{2-}** undergoes oxidative addition of halogens (chlorine and bromine) (**A**) analogous to oxidative addition of halogens to tetracyanoplatinate(II) (**B**). In the course of the reaction a very stable anion-π adduct is formed characterized by extremely short molecular contacts between the center of the C_6 ring of the **tripak^0** and the chloride anions (**A**).

DFT calculations of the interaction energies between halide anion(s) and π-acceptor **tripak^0** along with the subsequent ETS-NOCV [97,98] charge and energy decomposition analysis were performed for both **halide-tripak^0** (tripak/X^-) and **dihalide-tripak^0** (tripak/$2X^-$) contacts and, for a comparison, for the corresponding aforementioned reference motifs DDQ/Cl^- and HAT$(CN)_6$/Br^- extracted from the respective crystal structures. [99,100] The SI provides a visualization of all the considered assemblies (Figure S20, see also Figure 8B), a detailed description of computational methods and a full set of computed data (Figures S21-S26 and Tables S23-S24) with additional analyses. As shown in Table S23 in the SI, the calculated π-acceptor/anion interaction energy values do not demonstrate strong dependence on the density functional employed in the computations with the results obtained using double-hybrid functionals (expected to be the most accurate ones [101]) agreeing rather well with those from the standard DFT calculations (note that somewhat more pronounced differences were noticed for the reference systems) and more importantly with the energetic trends between the systems remaining always preserved (Table S23 in the SI). Namely, as illustrated in Table 3 (and Table S23 in the SI), the **halide-tripak^0** contacts exhibit strongly enhanced interaction energies as compared to their corresponding references (by ca. 33-40 and 23-31 kcal·mol^{-1} for Cl^- and Br^-, respectively), and among tripak-based assemblies, the ones with chloride show higher anion-π interaction strength than those with bromide (by ca. 2-4 and 8-12 kcal·mol^{-1} for tripak/X^- and tripak/$2X^-$, respectively). This is in line with the aforementioned trends in the halide-acceptor distances in the considered contacts, and, regarding the comparison with DDQ and HAT$(CN)_6$, with computed electrostatic potential (ESP) maps that reveal a significant π-electron density deficiency at (and around) the center of the aromatic ring(s) for both reference systems and tripak, which is however visibly increased for the latter (Figure 8A, blue-coded), reflecting its more effective ability to be anion's acceptor. The results of the ETS-NOCV analysis (Table 3, Figure 8B as well as Figures S21-S26 and Table S24 in the SI) confirm that the acceptor/anion interaction in the analyzed motifs is indeed dominated by the electrostatic interaction (ΔE_{elstat}) but indicate also almost equal importance

of the orbital-interaction component (ΔE_{orb}), which – as shown by the analysis of the dominant NOCV contributions to the differential electron density describing a change in the electron density around halide(s) and acceptor due to the anion-π interaction – is represented predominantly by charge-transfer (CT) type electron density flow from every π-lone-pair of halide anion(s) to the acceptor, combined with a strong anion-induced charge redistribution (polarization) within the acceptor, towards the periphery (electron-withdrawing substituents) of the molecule. While all the considered systems (both tripak-based and references) exhibit anion-π interactions of similar nature, dominated by both electrostatic and CT/polarization contributions, for DDQ/Cl^- and HAT$(CN)_6$/Br^- these effects appear to be drastically diminished (less stabilizing (negative) ΔE_{elstat} and ΔE_{orb} values) resulting in a lower strength of acceptor/anion interactions in these systems as compared to the corresponding motifs with tripak. It seems that higher strength of observed anion-π interactions in **halide-tripak^0** assemblies (vs. the reference systems) can be in fact traced back to an increase in the electron density deficiency observed in the ESP maps that leads to a stronger electrostatic interaction with the negatively charged ion and consequently a decrease in the anion-acceptor distance. The shortening of the distances guarantees more effective electron density transfer from the anion to the π-orbital system of tripak, which, combined with the subsequent redistribution of this density within the molecule results in the more stabilizing orbital-interaction energy. This amplifies the effect of a stronger electrostatic interaction and finally translates into the high strength of anion-π interactions for **halide-tripak^0** assemblies. Noteworthy, the strength of the anion-π interactions between **tripak** and halides does not seem to depend on the type of countercations or the crystal lattice - the respective acceptor-halide interaction energies and their components presented in Table S23-S24 in the SI are very similar for the tetrabutylammonium and tetraphenylphosphonium salts of tripak.

Table 3. Comparison of acceptor / halide-ion interaction energy values and their components as obtained from the ETS-NOCV analysis performed for the examined anion-π molecular adducts with BLYP+D4/TZ2P. Energies listed correspond to: ΔE_{int} – total interaction, ΔE_{orb} – orbital interaction, ΔE_{Pauli} – Pauli repulsion, ΔE_{elstat} – electrostatic interaction, and ΔE_{disp} – dispersion interaction. ΔE_i and q_i (i = 1, 2, 3) correspond to orbital interaction energy and charge measures for dominant NOCV contributions to $\Delta\rho_i$ (see Figure 8B). All energies are in kcal·mol^{-1} and charge in e^-.

Assembly	ΔE_{int}	ΔE_{orb}	ΔE_{Pauli}	ΔE_{elstat}	ΔE_{disp}	ΔE_i (q_i)		
						$\Delta\rho_1$	$\Delta\rho_2$	$\Delta\rho_3$
DDQ/Cl^-	-44.91	-32.26	23.10	-29.46	-6.29	-23.38 (0.796)	-2.78 (0.204)	-0.89 (0.103)
HAT$(CN)_6$/Br^-	-51.56	-24.78	16.78	-36.09	-7.47	-10.76 (0.629)	-3.83 (0.375)	-3.83 (0.375)
tripak^0/Cl^- (from **0c**)	-78.95	-64.72	72.77	-76.68	-10.33	-37.27 (0.821)	-10.11 (0.393)	-10.11 (0.393)
tripak^0/Br^- (from **0d**)	-75.20	-64.07	79.16	-78.57	-11.71	-39.76 (0.902)	-8.75 (0.399)	-8.74 (0.399)

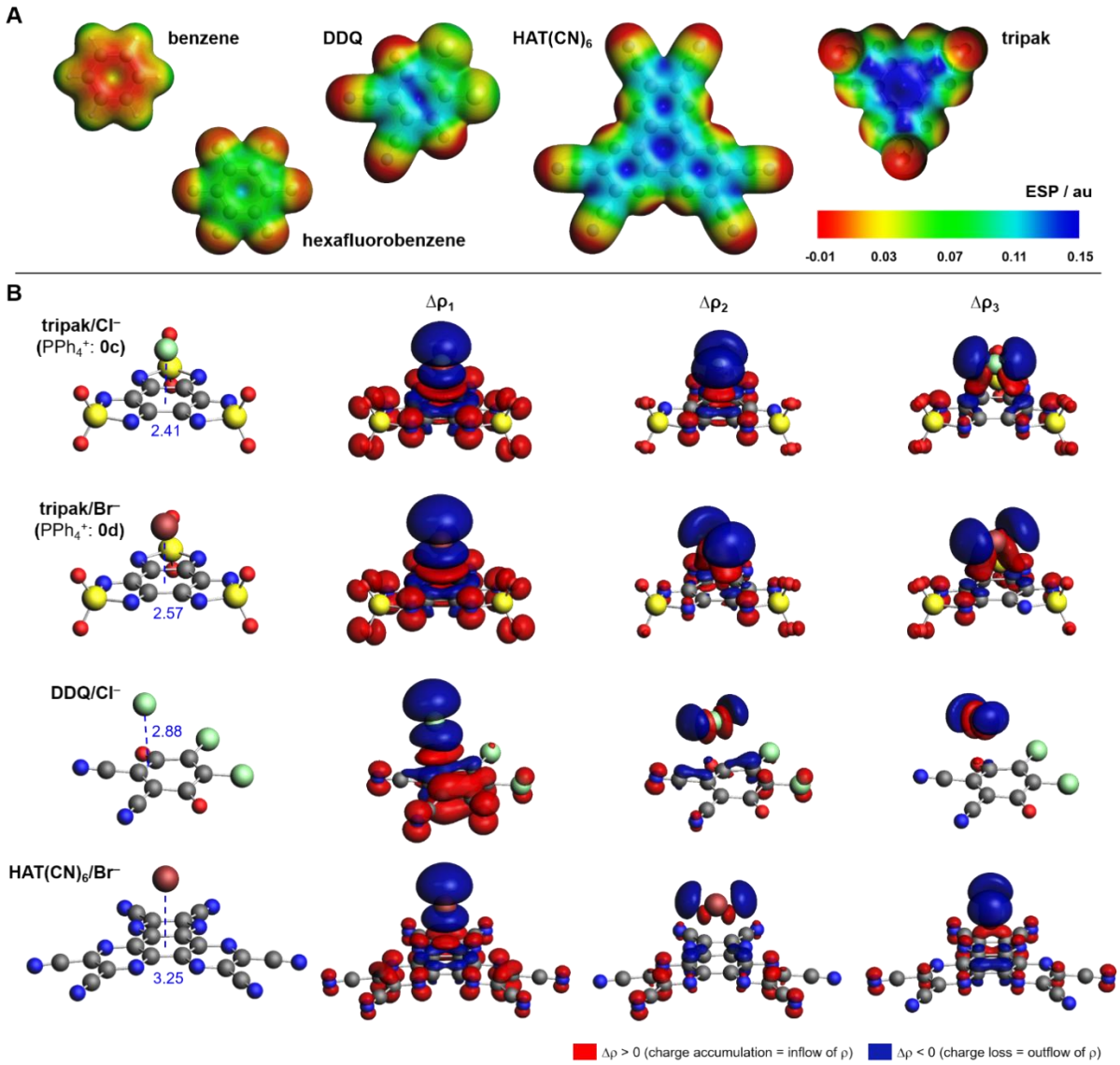

Fig. 8. Analysis of anion-π interactions in halide-tripak^0 assemblies and their reference systems. Comparison of the computed electrostatic potential (ESP) around benzene, hexafluorobenzene, DDQ, $HAT(CN)_6$ and tripak molecules mapped onto electron density isosurfaces with ρ = 0.008 au (**A**; electron-deficient and electron-rich regions are codded as blue and red, respectively). Isosurfaces of dominant NOCV contributions to $\Delta\rho$ (**B**) describing the interaction between halide anion and the π-acceptor molecule in the tripak/Cl^-, tripak/Br^-, DDQ/Cl^-, and $HAT(CN)_6/Br^-$ systems as extracted from the respective X-ray crystal structures (shown on the left along with the halide-centroid$_{ring/bond}$ distances, in Å). Red and blue colors indicate inflow (gain) and outflow (loss) of electron density, respectively. Presented results are based on BLYP+D4/TZ2P calculations.

Properties of the paramagnetic tripak^{1-} and tripak^{3-}

One electron oxidation or one electron reduction of the native form of tripak (**tripak^{2-}**) leads in both cases to an uneven electron count and hence a radical character of both species: **tripak^{1-}** and **tripak^{3-}**, respectively. This is clearly evidenced by the solution X-band EPR spectra for compounds containing **tripak^{1-}** and **tripak^{3-}** (Figure 9A-C). The solution EPR spectra of **1-a**, **1-b**, **3-a** and **3-b** all show strong signals with the *g*-factor close to 2.0023, typical for organic radicals. **3-a** (**tripak^{3-}**) gives a broad and featureless signal at g = 2.0039 only at low temperature (120 K) and the EPR spectrum of **3-b** (the

tetraphenylphosphonium salt) is basically identical. **1-a** and **1-b** (**tripak**$^{1-}$), on the other hand, show EPR signals centered at 2.0028 consisting of 13 extremely narrow major lines due to the hyperfine coupling to six equivalent nitrogen atoms of **tripak**$^{1-}$ with A_N = 5.36 MHz. Such narrow lines enable the observation of the hyperfine coupling even to low abundance ^{13}C carbon atoms with A_C = 4.61 MHz (the hyperfine coupling values are given for the THF solution of **1-b**) and correspond to an unusually long spin-spin relaxation time T_2 ≈ 0.9 µs (at room temperature). This was calculated based on the EPR spectrum of **1-b** using the formula [102]:

$$T_2 = \frac{2}{\sqrt{3}\gamma\Delta B_{pp}} \quad \text{Eq. 1}$$

where γ is the gyromagnetic ratio and ΔB_{pp} is the peak-to-peak linewidth of the first-derivative signal. This feature highlights the possibility of using **tripak**$^{1-}$ as a molecular qubit candidate at room temperature - a goal that is currently pursued in our laboratory. The observation of the EPR spectra for **tripak**$^{1-}$ and **tripak**$^{3-}$ is consistent with the lack of the ^{13}C NMR signal for the central C_6-ring for these species.

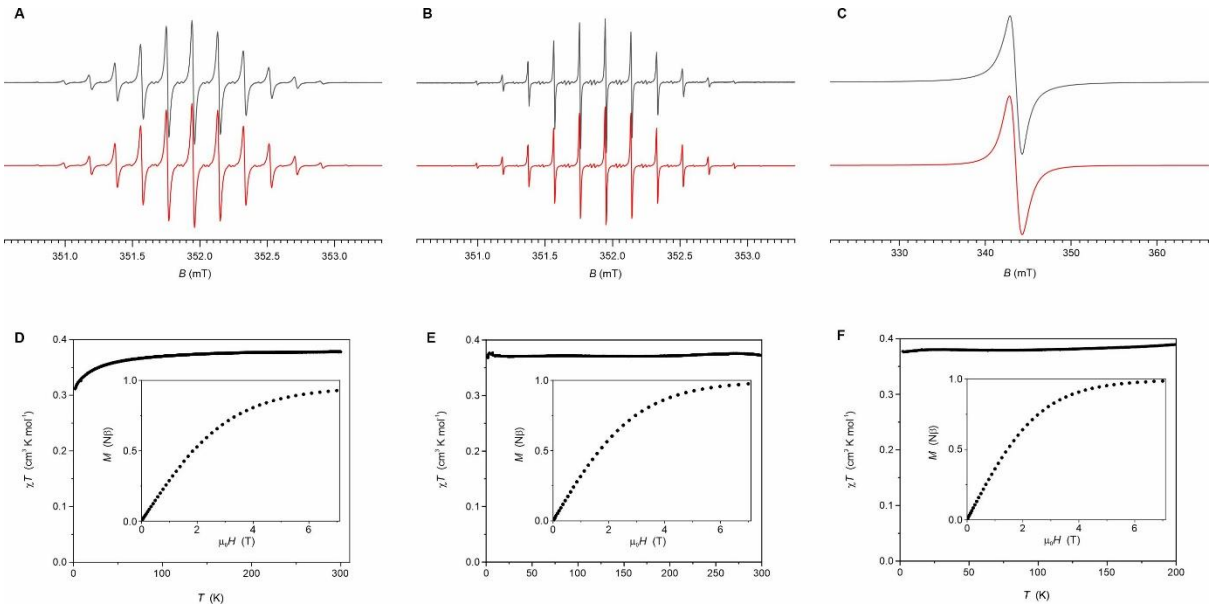

Fig. 9. X-band EPR spectra and magnetic properties of the tripak radicals. Experimental (black lines) and simulated (red lines) X-band EPR spectra for the tripak monoanions **1-a** (A), **1-b** (B) in THF at room temperature and for the trianion **3-a** (C) in THF at 120 K. $\chi T(T)$ recorded at 0.1 T (main plots) and $M(H)$ recorded at 2.0 K (insets) for the solid samples of **1-a** (D), **3-b** (E) and **3-a** (F).

In order to confirm the radical character of **tripak**$^{1-}$ and **tripak**$^{3-}$ in the solid state, variable temperature/field magnetic measurements were performed using SQUID magnetometer for **1-a**, **3-a** and **3-b** (Figures 9D-F). The temperature dependencies of the molar magnetic susceptibility and temperature product ($\chi T(T)$) for all three compounds show very similar behavior with the χT values remaining constant down to the lowest temperatures: 0.38 cm^3·K·mol^{-1} for **1-a**, 0.37 cm^3·K·mol^{-1} for **3-a** and 0.38 cm^3·K·mol^{-1} for **3-b** and typical for well-isolated isotropic S = 1/2 systems with the expected χT = 0.375 cm^3·K·mol^{-1} assuming g = 2.00. This is fully consistent with the results of the EPR measurements. Similar conclusions can be drawn from the analysis of the magnetic field dependencies of the molar magnetization (insets in Figure 9D-F). In all three cases the molar magnetization approaches the value of 1.00 Nβ (N - Avogadro number, β - Bohr magneton) expected for S = 1/2 paramagnets.

It should be noted that with the exception of phthalocyanine systems [103] and tppz [11] no other examples of ligands with two accessible paramagnetic states are present in the literature and both phthalocyanines and tppz offer limited coordination modes allowing for the preparation of dinuclear complexes at best. Moreover, these radical states are only obtained in a strongly reducing potential range ($tppz^{-1}/^{-3}$) or electrochemically (phthalocyanine). [104] Tripak is therefore one of the very few organic systems with two easily accessible paramagnetic states with one of them being stable in the presence of oxygen.

Properties of the tripak^{2-}

Similarly to the [6]oxocarbon dianion (rhodizonate dianion), the dianionic species **tripak^{2-}** is the native form of the reported system. As already mentioned, it shows a deep blue color with very large molar absorption coefficient in the UV-vis region: the strongest absorption band at λ_{max} = 608 nm reaches ε_{608nm} = 42 000 L·mol^{-1}·cm (THF solution; Figure 5C). In the case of MeCN solution: λ_{max} = 604 nm and in the solid state λ_{max} = 614 nm. This strong absorption is associated with the electronic transitions within the HOMO-LUMO orbitals of **tripak^{2-}** (Figure 4).

The strong absorption of **tripak^{2-}** in the form of the $(NBu_4)_2$tripak (**2-a**) is accompanied by red fluorescence with the maximum at 666 nm (MeCN solution; Figure 10A) or 715 nm (powder sample; Figure 10B) at room temperature. Interestingly, the fluorescence spectra are weakly dependent on the excitation wavelength with only small differences in the emission intensity (Figures 10C-D). At low temperature, the flourescence spectra of the solid sample of $(NBu_4)_2$tripak (**2-a**) shift towards higher energies (from 711 nm at RT to 657 nm at 77 K) and becomes well-resolved revealing vibrational fine structure (Figure 10D). The observed shift makes $(NBu_4)_2$tripak (**2-a**) a possible candidate for luminescence thermometry. Moreover, fluorescence lifetime in the solid state is 16.3 ± 0.1 ns which renders **tripak^{2-}** a possible fluorescent probe in time-resolved imaging that would mitigate the autofluorescence background from biological samples with lifetimes an order of magnitude lower. [105] Fluorescence quantum yields are ca. 0.01 for the solid and 0.02 for MeCN solution.

Stokes shift equals to 100 nm in the solid state and 62nm in MeCN. This is a rather large value indicating a possible use of this molecule as the fluorescent dye in fluorescence imaging techniques. All mentioned properties of **tripak^{2-}** except the quantum yield are comparable in this context with, for example, rubrene which is proposed as a standard for fluorescence lifetime measurements. [106]

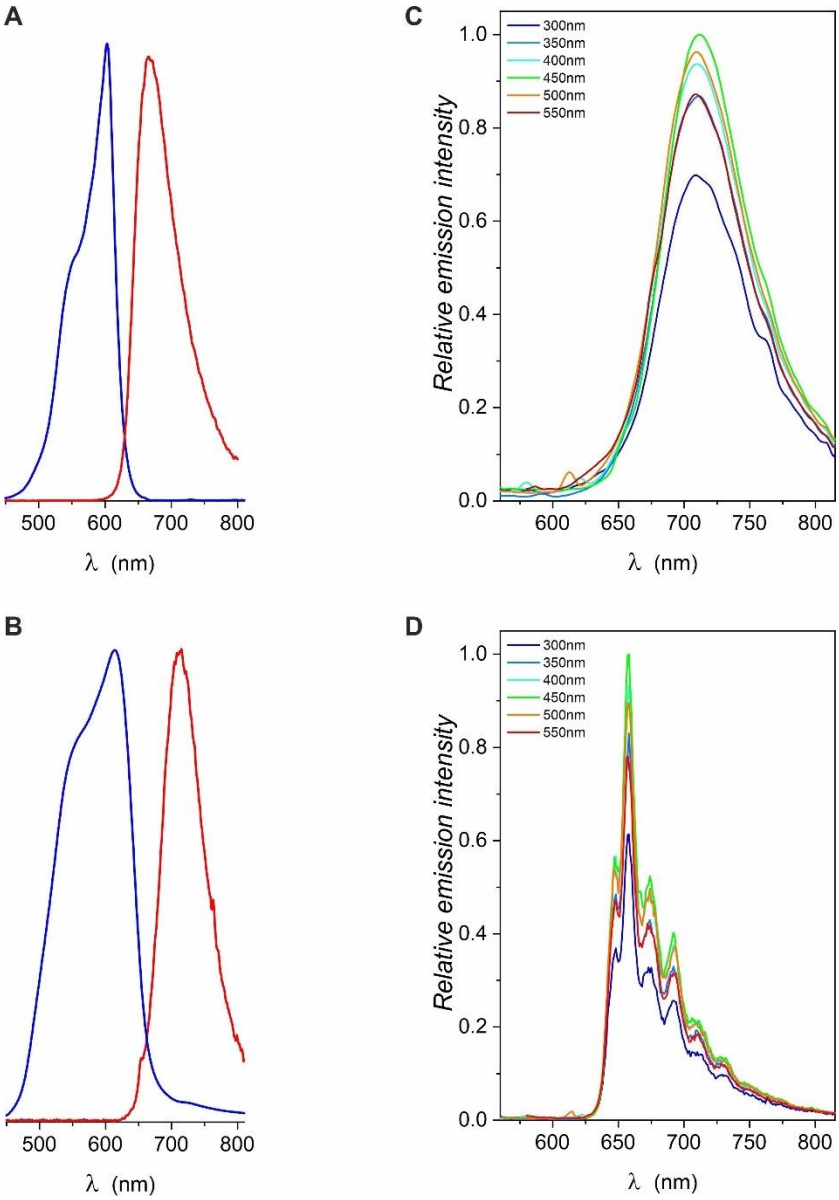

Fig. 10. Fluorescence of tripak^{2-}. Normalized absorption (blue line) and emission (red line) spectra of $(NBu_4)_2$tripak (**2-a**) at room temperature for MeCN solution (**A**) and powder (**B**). Excitation-emission maps for the solid sample of $(NBu_4)_2$tripak (**2-a**) at room temperature (**C**) and at 77 K (**D**).

Properties of the tripak^{4-}

Tripak^{4-} can be accessed via the chemical reduction of $(NBu_4)_2$tripak (**2-a**) or $(NBu_4)_3$tripak·THF (**3-a**) in benzene using KC_8. However, preparation using **2-a** as a starting material is preferred due to the better availability of this substrate. Interestingly, the substrate $(NBu_4)_2$tripak (**2-a**) does not appear to be soluble in benzene even in the presence of 2 eq. of NBu_4PF_6 but undergoes immediate reaction once the first portion of KC_8 is added. The reaction is completed within several minutes and produces an orange solution containing the desired product and the crystalline KPF_6. Removal of benzene yields crude product as an orange powder which recrystallizes from THF in the form of dark-orange prismatic crystals of $(NBu_4)_4$tripak·2THF (**4-a**). Noteworthy, the tetraanionic **tripak^{4-}** in its tetrabutylammonium salt exhibits much higher solubility in non-polar solvents such as benzene or toluene than the parent dianionic substrate **tripak^{2-}**. This might be rationalized by the effect of the four tetrabutylammonium

cations which seem to form an aliphatic pocket matching perfectly the small **tripak**$^{4-}$. This enveloping effect is clearly seen in the crystal structure of **4-a**.

The geometry optimizations for the **tripak**$^{4-}$ anion in the gas phase suggest a triplet ground state (S = 1) with a perfectly trigonal symmetry (point group D_{3h}) and the calculated triplet-singlet close to zero. However, the analysis of the crystal structure of the actual tetrabutylammonium salt **4-a** shows a clear deviation of the **tripak**$^{4-}$ skeleton from the idealized D_{3h} symmetry towards C_{2v} with elongation and shortening of the respective bonds within its molecular skeleton and an unusually large distribution of these bond lengths (see Figures S15-S19 in the SI). According to the results of the DFT calculations, such a large distribution is not consistent with the **tripak**$^{4-}$ in the triplet state (D_{3h} symmetry) nor open-shell spin-singlet but fully complies with the closed-shell singlet configuration (C_{2v} symmetry). For closed-shell configuration, however, external instability of the wavefunction was detected. On the other hand, the single-point energy calculations at the experimental structure of **tripak**$^{4-}$ as found in compound **4-a** confirmed that at such distorted geometry the open-shell spin-singlet electronic configuration is preferred over the pure spin-triplet with nearly zero singlet-triplet gap. In other words, the **tripak**$^{4-}$ anion in **4-a** is a diradicaloid system with the mixture of singlet and triplet states in its ground state, dominated, however, by the former S = 0 state. It is therefore not surprising that **4-a** is EPR silent and shows zero magnetic moment. Nevertheless, a non-negligible onset of the magnetic moment up to 0.05 $cm^3 \cdot K \cdot mol^{-1}$ was observed when the sample was heated above room temperature, which might indicate an increased admixture of the magnetic triplet state in accordance with the results of the theoretical calculations discussed above. Unfortunately, **4-a** exhibits relatively low decomposition temperature of ca. 100 °C (see TGA results presented in Figure S27 in the SI), which prevents a more detailed study of the $\chi T(T)$ dependence for this particular **tripak**$^{4-}$ salt. Interestingly, ^{13}C NMR spectra in MeCN at RT do not show the presence of the carbon signal of the C_6 ring of **tripak**$^{4-}$. Such a behavior is typical for compounds with unpaired electrons e.g., **tripak**$^{1-}$ and **tripak**$^{3-}$ and supports non-zero population of the spin-triplet state also at room temperature.

Conclusions

A single dioxothiadiazole group attached to a graphenoid skeleton is capable of accepting up to two electrons. Herein, we have presented an organic molecule in which three such groups are fused into a single benzenoid ring forming a *pseudo*-[6]oxocarbon species with the ability to accept up to six electrons within its simple triangular skeleton. All six oxidation states are easily accessible within the electrochemical window of common organic solvents. The resulting multi-redox **tripak** system was successfully isolated in five-out-of-six available oxidation states and studied using a wide range of techniques including scXRD structural analysis. The latter revealed a systematic swelling/shrinking of the respective bonds with each additional electron "injected" into the LUMO levels of the molecule in the consecutive reduction steps. Such a behavior is not unexpected and yet it was never observed/demonstrated before due to the lack of a suitably robust organic multi-redox system. **Tripak** is the first clear textbook example of multi-redox behavior with fully documented variation of structural, physical and chemical properties. The possibility of injecting up to six electrons and the isolation of five different oxidation states provided the unique opportunity to observe three different aromaticity types, two different radical states and the diradicaloid state within the same simple molecular framework consisting of only 21 atoms. As demonstrated, each additional electron injected into the **tripak** skeleton unlocks additional functionalities beginning with the record strong halide binding, through two radical and one diradicaloid state to fluorescence and strong visible light absorption. Finally, the tripak system is the first example of the new family of poly(dioxothiadiazoles) – organic compounds with embedded multi-redox behavior.

Acknowledgments

This work was financed by the European Union within the Horizon Europe Framework Programme, ERC Consolidator Grant LUX-INVENTA no. 101045004 and by National Science Centre Poland within the Preludium project no. 2021/41/N/ST5/04375. SD is grateful to the Department of Chemistry at Michigan State University (MSU) for generous start-up funds. PP acknowledges the Kosciuszko Foundation, the American Centre of Polish Culture for the financial support of his stay in at MSU. The study was carried out using the research infrastructure cofounded by the European Union in the framework of the Smart Growth Operational Program, Measure 4.2; Grant No. POIR.04.02.00-00-D001/20, "ATOMIN 2.0 – ATOMic scale science for the INnovative economy". We gratefully acknowledge Polish high-performance computing infrastructure PLGrid (HPC Centers: ACK Cyfronet AGH) for providing computer facilities and support within computational grants no. PLG/2021/015125 and PLG/2022/015911.

References

1. Hieber, W.; Braun, G. Notizen; „Rheniumcarbonylwasserstoff" Und Methylpentacarbonylrhenium. *Zeitschrift fur Naturforschung - Section B Journal of Chemical Sciences* **1959**, *14*, 132–133, doi:10.1515/znb-1959-0214.

2. Strong, H.; Krusic, P.J.; Filippo, J.S.; Keenan, S.; Finke, R.G. Sodium Carbonyl Ferrates, Na 2 [Fe(Co) 4], Na 2 [Fe 2 (Co) 8], and Na 2 [Fe 3 (Co) 11]. Bis[μ - Nitrido-Bis(Triphenylphosphorus)(1 +)] Undeca-Carbonyltriferrate(2-), [(Ph 3 P) 2 N] 2 [Fe 3 (Co) 11] . In *Inorganic Syntheses*; Inorganic Syntheses; 2007; pp. 203–207 ISBN 9780470132593.

3. Anema, S.G.; Barris, G.C.; Mackay, K.M.; Nicholson, B.K. Improved Syntheses of M[Fe2(CO)8]2 (M = Si, Ge or Sn) and the X-Ray Crystal Structure of Si[Fe2(CO)8]2. *J Organomet Chem* **1988**, *350*, 207–215, doi:10.1016/0022-328X(88)80376-0.

4. Mond, L.; Langer, C. XCIII. - On Iron Carbonyls. *Journal of the Chemical Society, Transactions* **1891**, *59*, 1090–1093, doi:10.1039/CT8915901090.

5. Piper, T.S.; Cotton, F.A.; Wilkinson, G. Cyclopentadienyl-Carbon Monoxide and Related Compounds of Some Transitional Metals. *Journal of Inorganic and Nuclear Chemistry* **1955**, *1*, 165–174, doi:10.1016/0022-1902(55)80053-X.

6. Tomyn, S.; Shylin, S.I.; Bykov, D.; Ksenofontov, V.; Gumienna-Kontecka, E.; Bon, V.; Fritsky, I.O. Indefinitely Stable Iron(IV) Cage Complexes Formed in Water by Air Oxidation. *Nat Commun* **2017**, *8*, 14099, doi:10.1038/ncomms14099.

7. Demazeau, G.; Buffat, B.; Pouchard, M.; Hagenmuller, P. Recent Developments in the Field of High Oxidation States of Transition Elements in Oxides Stabilization of Six-coordinated Iron(V). *ZAAC - Journal of Inorganic and General Chemistry* **1982**, *491*, 60–66, doi:10.1002/zaac.19824910109.

8. De Oliveira, F.T.; Chanda, A.; Banerjee, D.; Shan, X.; Mondal, S.; Que, L.; Bominaar, E.L.; Münck, E.; Collins, T.J. Chemical and Spectroscopic Evidence for an FeV-Oxo Complex. *Science (1979)* **2007**, *315*, 835–838, doi:10.1126/science.1133417.

9. Licht, S.; Yu, X. Recent Advances in Fe(VI) Synthesis. In *ACS Symposium Series*; ACS Symposium Series; American Chemical Society, 2008; Vol. 985, pp. 2–51 ISBN 9780841269613.

10. Deuchert, K.; Hünig, S. Multistage Organic Redox Systems—A General Structural Principle. *Angewandte Chemie International Edition in English* **1978**, *17*, 875–886, doi:10.1002/anie.197808753.

11. Demir, S.; Nippe, M.; Gonzalez, M.I.; Long, J.R. Exchange Coupling and Magnetic Blocking in Dilanthanide Complexes Bridged by the Multi-Electron Redox-Active Ligand 2,3,5,6-Tetra(2-Pyridyl)Pyrazine. *Chem Sci* **2014**, *5*, 4702–4711, doi:10.1039/c4sc02154a.

12. Ma, X.; Suturina, E.A.; De, S.; Négrier, P.; Rouzières, M.; Clérac, R.; Dechambenoit, P. A Redox-Active Bridging Ligand to Promote Spin Delocalization, High-Spin Complexes, and Magnetic Multi-Switchability. *Angewandte Chemie - International Edition* **2018**, *57*, 7841–7845, doi:10.1002/anie.201803842.

13. Han, Z.; Vaid, T.P.; Rheingold, A.L. Hexakis(4-(N-Butylpyridylium))Benzene: A Six-Electron Organic Redox System. *Journal of Organic Chemistry* **2008**, *73*, 445–450, doi:10.1021/jo701944c.

14. Antoni, P.W.; Golz, C.; Hansmann, M.M. Organic Four-Electron Redox Systems Based on Bipyridine and Phenanthroline Carbene Architectures. *Angewandte Chemie - International Edition* **2022**, *61*, e202203064, doi:10.1002/anie.202203064.

15. Goswami, S.; Rath, S.P.; Thompson, D.; Hedström, S.; Annamalai, M.; Pramanick, R.; Ilic, B.R.; Sarkar, S.; Hooda, S.; Nijhuis, C.A.; et al. Charge Disproportionate Molecular Redox for Discrete Memristive and Memcapacitive Switching. *Nat Nanotechnol* **2020**, *15*, 380–389, doi:10.1038/s41565-020-0653-1.

16. Cabrera, P.J.; Yang, X.; Suttil, J.A.; Hawthorne, K.L.; Brooner, R.E.M.; Sanford, M.S.; Thompson, L.T. Complexes Containing Redox Noninnocent Ligands for Symmetric, Multielectron Transfer Nonaqueous Redox Flow Batteries. *The Journal of Physical Chemistry C* **2015**, *119*, 15882–15889, doi:10.1021/acs.jpcc.5b03582.

17. Chen, J.-J.; Symes, M.D.; Cronin, L. Highly Reduced and Protonated Aqueous Solutions of [P2W18O62]6− for on-Demand Hydrogen Generation and Energy Storage. *Nat Chem* **2018**, *10*, 1042–1047, doi:10.1038/s41557-018-0109-5.

18. Bernardini, G.; Wedd, A.G.; Zhao, C.; Bond, A.M. Electrochemical Probing of the Photoreduction of Molybdenum and Tungsten Dawson-Type Polyoxometalates

in Molecular and Ionic Liquid Media Using Water as an Electron Donor. *Dalton Transactions* **2012**, *41*, 9944–9954, doi:10.1039/c2dt30558e.

19. Zhang, J.; Bond, A.M.; MacFarlane, D.R.; Forsyth, S.A.; Pringle, J.M.; Mariotti, A.W.A.; Glowinski, A.F.; Wedd, A.G. Voltammetric Studies on the Reduction of Polyoxometalate Anions in Ionic Liquids. *Inorg Chem* **2005**, *44*, 5123–5132, doi:10.1021/ic050032t.

20. Richardt, P.J.S.; White, J.M.; Tregloan, P.A.; Bond, A.M.; Wedd, A.G. One-Electron Reduction of the Γ*-Isomer of [S2W18O62]4- Leads to Isolation of the α-Isomer. *Can J Chem* **2001**, *79*, 613–620, doi:10.1139/v01-010.

21. Hori, T.; Tamada, O.; Himeno, S. The Structure of 18-Molybdodisulphate(VI)(4-) Ion in (NEt4)4S2Mo18O 62·CH3CN. *Journal of the Chemical Society, Dalton Transactions* **1989**, 1491–1497, doi:10.1039/DT9890001491.

22. Neier, R.; Trojanowski, C.; Mattes, R. Reduced Polyoxomolybdates with the Keggin and Dawson Structures: Preparation and Crystal Structures of Two-Electron Reduced [K(18-Crown-6)]2[N(PPh3)2] 2[HPMo12O40]·8MeCN·18-Crown-6 and Four-Electron Reduced [NBun4]5[H3S2Mo 18O62]... *Journal of the Chemical Society, Dalton Transactions* **1995**, 2521–2528, doi:10.1039/DT9950002521.

23. SUN Yue-Xia, ZHANG Zhi-Bin, SUN Qi, X.Y. Syntheses, Characterization and Catalytic Properties of Two New Wells-Dawson Molybdosulfates. *Chinese Journal of Inorganic Chemistry* **2011**, *27*, 556–560, doi:10.5517/ccv959l.

24. Naghibi, S.; Sangtarash, S.; Kumar, V.J.; Wu, J.-Z.; Judd, M.M.; Qiao, X.; Gorenskaia, E.; Higgins, S.J.; Cox, N.; Nichols, R.J.; et al. Redox-Addressable Single-Molecule Junctions Incorporating a Persistent Organic Radical**. *Angewandte Chemie International Edition* **2022**, *61*, e202116985, doi:https://doi.org/10.1002/anie.202116985.

25. Goswami, S.; Pramanick, R.; Patra, A.; Rath, S.P.; Foltin, M.; Ariando, A.; Thompson, D.; Venkatesan, T.; Goswami, S.; Williams, R.S. Decision Trees within a Molecular Memristor. *Nature* **2021**, *597*, 51–56, doi:10.1038/s41586-021-03748-0.

26. Huang, J.; Hu, S.; Yuan, X.; Xiang, Z.; Huang, M.; Wan, K.; Piao, J.; Fu, Z.; Liang, Z. Radical Stabilization of a Tripyridinium–Triazine Molecule Enables Reversible Storage of Multiple Electrons. *Angewandte Chemie International Edition* **2021**, *60*, 20921–20925, doi:https://doi.org/10.1002/anie.202107216.

27. Antoni, P.W.; Golz, C.; Hansmann, M.M. Organic Four-Electron Redox Systems Based on Bipyridine and Phenanthroline Carbene Architectures. *Angewandte Chemie International Edition* **2022**, *61*, e202203064, doi:https://doi.org/10.1002/anie.202203064.

28. Lin, Q.; Li, H.; Chen, L.; He, X. Naphthalenediimide-Carbonylpyridiniums: Stable Six Electron Acceptors for Organic Cathodes. *Mater Chem Front* **2023**, doi:10.1039/D3QM00501A.

29. Zhang, J.; Bond, A.M.; Richardt, P.J.S.; Wedd, A.G. Voltammetric Reduction of α- and Γ*- [S2W 18O62]4- and α-, β-, and γ-[SiW12O40]4-: Isomeric Dependence of Reversible Potentials of Polyoxometalate Anions Using Data Obtained by Novel Dissolution and Conventional Solution-Phase Processes. *Inorg Chem* **2004**, *43*, 8263–8271, doi:10.1021/ic049043x.

30. Himeno, S.; Tatewaki, H.; Hashimoto, M. Synthesis, Structure, and Characterization of an α-Dawson-Type [S 2W 18O 62] 4- Complex. *Bull Chem Soc Jpn* **2001**, *74*, 1623–1628, doi:10.1246/bcsj.74.1623.

31. Michaelis, L. Ein Reduktions-Indikator Im Potentialbereich Der Wasserstoffuberspannung. *Biochem Z* **1932**, *250*, 564–567.

32. Michaelis, L.; Hill, E.S. The Viologen Indicators. *Journal of General Physiology* **1933**, *16*, 859–873, doi:10.1085/jgp.16.6.859.

33. Canevet, D.; Sallé, M.; Zhang, G.; Zhang, D.; Zhu, D. Tetrathiafulvalene (TTF) Derivatives: Key Building-Blocks for Switchable Processes. *Chemical Communications* **2009**, 2245–2269, doi:10.1039/b818607n.

34. Martín, N.; Segura, J.L.; Seoane, C. Design and Synthesis of TCNQ and DCNQI Type Electron Acceptor Molecules as Precursors for "Organic Metals." *J Mater Chem* **1997**, *7*, 1661–1676, doi:10.1039/a702314f.

35. Coleman, L.B.; Cohen, M.J.; Sandman, D.J.; Yamagishi, F.G.; Garito, A.F.; Heeger, A.J. Superconducting Fluctuations and the Peierls Instability in an Organic Solid. *Solid State Commun* **1973**, *12*, 1125–1132, doi:10.1016/0038-1098(73)90127-0.

36. Bryce, M.R.; Murphy, L.C. Organic Metals. *Nature* **1984**, *309*, 119–126, doi:10.1038/309119a0.

37. González, M.; De Miguel, P.; Martin, N.; Segura, J.L.; Seoane, C.; Orti, E.; Viruela, R.; Viruela, P.M. The First Sulfur-containing Twin-DCNQI-type Acceptor. *Advanced Materials* **1994**, *6*, 765–768, doi:10.1002/adma.19940061011.

38. Jerome, D.; Mazaud, A.; Ribault, M.; Bechgaard, K. Superconductivity in a Synthetic Organic Conductor (Tmtsf)2Pf6. *Journal de physique. Lettres* **1980**, *41*, 95–98, doi:10.1051/jphyslet:0198000410409500.

39. Williams, J.M.; Schultz, A.J.; Geiser, U.; Carlson, K.D.; Kini, A.M.; Wang, H.H.; Kwok, W.K.; Whangbo, M.H.; Schirber, J.E. Organic Superconductors - New Benchmarks. *Science (1979)* **1991**, *252*, 1501–1508, doi:10.1126/science.252.5012.1501.

40. Nguyen, T.P.; Easley, A.D.; Kang, N.; Khan, S.; Lim, S.M.; Rezenom, Y.H.; Wang, S.; Tran, D.K.; Fan, J.; Letteri, R.A.; et al. Polypeptide Organic Radical Batteries. *Nature* **2021**, *593*, 61–66, doi:10.1038/s41586-021-03399-1.

41. Matsunaga, T.; Kubota, T.; Sugimoto, T.; Satoh, M. High-Performance Lithium Secondary Batteries Using Cathode Active Materials of Triquinoxalinylenes Exhibiting Six Electron Migration. *Chem Lett* **2011**, *40*, 750–752, doi:10.1246/cl.2011.750.

42. Rossignon Beatrice Berionni; Parola A. Jorge; Laia César A. T.; Bonifazi Davide, A.B. HOMO Energy-Level Lifting in p-Type O-Doped Graphenoids: Synthesis of Electrochromic Alkoxy-Decorated Xanthenoxanthenes. *Organic Materials* **2022**, *4*, 240–254, doi:10.1055/a-1976-0291.

43. Yee, G.T.; McLean, R.S.; Epstein, A.J.; Miller, J.S. A Room-Temperature Molecular/Organic-Based Magnet. *Science (1979)* **1991**, *252*, 1415–1417, doi:10.1126/science.252.5011.1415.

44. Perlepe, P.; Oyarzabal, I.; Mailman, A.; Yquel, M.; Platunov, M.; Dovgaliuk, I.; Rouzières, M.; Négrier, P.; Mondieig, D.; Suturina, E.A.; et al. Metal-Organic Magnets with Large Coercivity and Ordering Temperatures up to 242°C. *Science (1979)* **2020**, *370*, 587–592, doi:10.1126/SCIENCE.ABB3861.

45. Gomberg, M. An Instance of Trivalent Carbon: Triphenylmethyl. *J Am Chem Soc* **1900**, *22*, 757–771, doi:10.1021/ja02049a006.

46. Hicks, R.G. *Stable Radicals: Fundamentals and Applied Aspects of Odd-Electron Compounds*; 2010; ISBN 9780470770832.

47. Ratera, I.; Veciana, J. Playing with Organic Radicals as Building Blocks for Functional Molecular Materials. *Chem Soc Rev* **2012**, *41*, 303–349, doi:10.1039/c1cs15165g.

48. Kato, K.; Osuka, A. Platforms for Stable Carbon-Centered Radicals. *Angewandte Chemie - International Edition* **2019**, *58*, 8978–8986, doi:10.1002/anie.201900307.

49. Chen, Z.X.; Li, Y.; Huang, F. Persistent and Stable Organic Radicals: Design, Synthesis, and Applications. *Chem* **2021**, *7*, 288–332, doi:https://doi.org/10.1016/j.chempr.2020.09.024.

50. Wang, Y.; Frasconi, M.; Stoddart, J.F. Introducing Stable Radicals into Molecular Machines. *ACS Cent Sci* **2017**, *3*, 927–935, doi:10.1021/acscentsci.7b00219.

51. Huang, B.; Kang, H.; Zhang, C.W.; Zhao, X.L.; Shi, X.; Yang, H.B. Design of an Open-Shell Nitrogen-Centered Diradicaloid with Tunable Stimuli-Responsive Electronic Properties. *Commun Chem* **2022**, *5*, 127, doi:10.1038/s42004-022-00747-8.

52. Ni, Y.; Gopalakrishna, T.Y.; Phan, H.; Kim, T.; Herng, T.S.; Han, Y.; Tao, T.; Ding, J.; Kim, D.; Wu, J. 3D Global Aromaticity in a Fully Conjugated Diradicaloid Cage at Different Oxidation States. *Nat Chem* **2020**, *12*, 242–248, doi:10.1038/s41557-019-0399-2.

53. Wang, T.; Berdonces-Layunta, A.; Friedrich, N.; Vilas-Varela, M.; Calupitan, J.P.; Pascual, J.I.; Peña, D.; Casanova, D.; Corso, M.; de Oteyza, D.G. Aza-Triangulene: On-Surface Synthesis and Electronic and Magnetic Properties. *J Am Chem Soc* **2022**, *144*, 4522–4529, doi:10.1021/jacs.1c12618.

54. Alcón, I.; Calogero, G.; Papior, N.; Antidormi, A.; Song, K.; Cummings, A.W.; Brandbyge, M.; Roche, S. Unveiling the Multiradical Character of the

Biphenylene Network and Its Anisotropic Charge Transport. *J Am Chem Soc* **2022**, *144*, 8278–8285, doi:10.1021/jacs.2c02178.

55. Gould, C.A.; McClain, K.R.; Reta, D.; Kragskow, J.G.C.; Marchiori, D.A.; Lachman, E.; Choi, E.S.; Analytis, J.G.; Britt, R.D.; Chilton, N.F.; et al. Ultrahard Magnetism from Mixed-Valence Dilanthanide Complexes with Metal-Metal Bonding. *Science (1979)* **2022**, *375*, 198–202, doi:10.1126/science.abl5470.

56. Gould, C.A.; Mu, E.; Vieru, V.; Darago, L.E.; Chakarawet, K.; Gonzalez, M.I.; Demir, S.; Long, J.R. Substituent Effects on Exchange Coupling and Magnetic Relaxation in 2,2'-Bipyrimidine Radical-Bridged Dilanthanide Complexes. *J Am Chem Soc* **2020**, *142*, 21197–21209, doi:10.1021/jacs.0c10612.

57. Demir, S.; Gonzalez, M.I.; Darago, L.E.; Evans, W.J.; Long, J.R. Giant Coercivity and High Magnetic Blocking Temperatures for N23- Radical-Bridged Dilanthanide Complexes upon Ligand Dissociation /639/638/263/406 /639/638/911 /639/638/298/920 Article. *Nat Commun* **2017**, *8*, 2144, doi:10.1038/s41467-017-01553-w.

58. Mahmood, J.; Park, J.; Shin, D.; Choi, H.-J.; Seo, J.-M.; Yoo, J.-W.; Baek, J.-B. Organic Ferromagnetism: Trapping Spins in the Glassy State of an Organic Network Structure. *Chem* **2018**, *4*, 2357–2369, doi:https://doi.org/10.1016/j.chempr.2018.07.006.

59. Steffenfauseweh, H.; Rottschäfer, D.; Vishnevskiy, Y. V; Neumann, B.; Stammler, H.-G.; Szczepanik, D.W.; Ghadwal, R.S. Isolation of an Annulated 1,4-Distibabenzene Diradicaloid. *Angewandte Chemie International Edition* **2023**, *n/a*, e202216003, doi:https://doi.org/10.1002/anie.202216003.

60. Dinnebier, R.E.; Nuss, H.; Jansen, M. Disodium Rhodizonate: A Powder Diffraction Study. *Acta Crystallogr Sect E Struct Rep Online* **2005**, *61*, m2148--m2150, doi:10.1107/S1600536805030552.

61. Cowan, J.A.; Howard, J.A.K. Dipotassium Rhodizonate. *Acta Crystallogr Sect E Struct Rep Online* **2004**, *60*, m511--m513, doi:10.1107/S160053680400529X.

62. Braga, D.; Cojazzi, G.; Maini, L.; Grepioni, F. Reversible Solid-State Interconversion of Rhodizonic Acid H2C6O6 into H6C6O8 and the Solid-State Structure of the Rhodizonate Dianion C6O62- (Aromatic or Non-Aromatic?). *New Journal of Chemistry* **2001**, *25*, 1221–1223, doi:10.1039/b107317f.

63. Linder, T.; Badiola, E.; Baumgartner, T.; Sutherland, T.C. Synthesis of π-Extended Thiadiazole (Oxides) and Their Electronic Properties. *Org Lett* **2010**, *12*, 4520–4523, doi:10.1021/ol1018213.

64. Seitz, G.; Imming, P. Oxocarbons and Pseudooxocarbons. *Chem Rev* **1992**, *92*, 1227–1260, doi:10.1021/cr00014a004.

65. Pakulski, P.; Pinkowicz, D. 1,2,5-Thiadiazole 1,1-Dioxides and Their Radical Anions: Structure, Properties, Reactivity, and Potential Use in the Construction of Functional Molecular Materials. *Molecules* **2021**, *26*, 4873, doi:10.3390/molecules26164873.

66. Eistert, B.; Fink, H.; Werner, H. -K Phenazin-Derivate Aus Rhodizonsäure. *Justus Liebigs Ann Chem* **1962**, *657*, 131–141, doi:10.1002/jlac.19626570118.

67. Andersen, J.; Mack, J. Mechanochemistry and Organic Synthesis: From Mystical to Practical. *Green Chemistry* **2018**, *20*, 1435–1443, doi:10.1039/c7gc03797j.

68. Bowmaker, G.A. Solvent-Assisted Mechanochemistry. *Chemical Communications* **2013**, *49*, 334–348, doi:10.1039/c2cc35694e.

69. Bakthadoss, M.; Selvakumar, R.; Srinivasan, J. An Efficient Protocol for the Synthesis of Benzoheterocyclic Compounds via Solid-State Melt Reaction (SSMR). *Tetrahedron Lett* **2014**, *55*, 5808–5812, doi:10.1016/j.tetlet.2014.08.084.

70. Gediz Erturk, A.; Bekdemir, Y. Microwave-Assisted Synthesis of Some Substituted Sulfamides. *Phosphorus Sulfur Silicon Relat Elem* **2014**, *189*, 285–292, doi:10.1080/10426507.2013.819868.

71. Wright, J.B. The Reaction of Sulfamide with α- and β-Diketones. The Preparation of 1,2,5-Thiadiazole 1,1-Dioxides and 1,2,6-Thiadiazine 1,1-Dioxides. *J Org Chem* **1964**, *29*, 1905–1909, doi:10.1021/jo01030a059.

72. Shuku, Y.; Suizu, R.; Awaga, K. Monovalent and Mixed-Valent Potassium Salts of [1,2,5]Thiadiazolo[3,4-f][1, 10]Phenanthroline 1,1-Dioxide: A Radical Anion for Multidimensional Network Structures. *Inorg Chem* **2011**, *50*, 11859–11861, doi:10.1021/ic201966t.

73. Pinkowicz, D.; Li, Z.; Pietrzyk, P.; Rams, M. New Thiadiazole Dioxide Bridging Ligand with a Stable Radical Form for the Construction of Magnetic Coordination Chains. *Cryst Growth Des* **2014**, *14*, 4878–4881, doi:10.1021/cg500906w.

74. Pakulski, P.; Arczyński, M.; Pinkowicz, D. Bis(Triphenylphosphine)Iminium Salts of Dioxothiadiazole Radical Anions: Preparation, Crystal Structures, and Magnetic Properties. *Crystals (Basel)* **2019**, *9*, 30, doi:10.3390/cryst9010030.

75. Arroyo, N.R.; Rozas, M.F.; Vázquez, P.; Romanelli, G.P.; Mirífico, M. V. Solvent-Free Condensation Reactions to Synthesize Five-Membered Heterocycles Containing the Sulfamide Fragment. *Synthesis (Germany)* **2016**, *48*, 1344–1352, doi:10.1055/s-0035-1561371.

76. Jiao, H.; Wu, H.S. Are Neutral Oxocarbons Stable? *Journal of Organic Chemistry* **2003**, *68*, 1475–1479, doi:10.1021/jo026243m.

77. Von Ragué Schleyer, P.; Najafian, K.; Kiran, B.; Jiao, H. Are Oxocarbon Dianions Aromatic? *Journal of Organic Chemistry* **2000**, *65*, 426–431, doi:10.1021/jo991267n.

78. de la Hoz, A.; Díaz-Ortiz, À.; Moreno, A. Microwaves in Organic Synthesis. Thermal and Non-Thermal Microwave Effects. *Chem Soc Rev* **2005**, *34*, 164–178, doi:10.1039/b411438h.

79. Garrett, M.; Tao, T.; Jolly, W.L. The Protonation and Deprotonation of Sulfamide and Sulfamate in Aqueous Solutions. *Journal of Physical Chemistry* **1964**, *68*, 824–826, doi:10.1021/j100786a020.

80. Connelly, N.G.; Geiger, W.E. Chemical Redox Agents for Organometallic Chemistry. *Chem Rev* **1996**, *96*, 877–910, doi:10.1021/cr940053x.

81. Vanýsek, P. Electrochemical Series. In *CRC Handbook of Chemistry and Physics*; Haynes, W.M., Ed.; CRC Press, 2016; pp. 578–584 ISBN 9781315380476.

82. Nelson, I. V.; Iwamoto, R.T. Voltammetric Evaluation of the Stability of Trichloride, Tribromide, and Triiodide Ions in Nitromethane, Acetone, and Acetonitrile. *Journal of Electroanalytical Chemistry* **1964**, *7*, 218–221, doi:10.1016/0022-0728(64)80015-2.

83. Sawyer, D.T.; Sobkowiak, A.; Roberts, J.L. *Electrochemistry for Chemists*; 2nd ed.; Wiley, 1995;

84. Datta, J.; Bhattacharya, A.; Kundu, K.K. Relative Standard Electrode Potentials of I3−/I−, I2/I3−, and I2/I− Redox Couples and the Related Formation Constants of I3− in Some Pure and Mixed Dipolar Aprotic Solvents. *Bull Chem Soc Jpn* **1988**, *61*, 1735–1742, doi:10.1246/bcsj.61.1735.

85. Kochi, J.K. Inner-Sphere Electron Transfer in Organic Chemistry. Relevance to Electrophilic Aromatic Nitration. *Acc Chem Res* **1992**, *25*, 39–47, doi:10.1021/ar00013a006.

86. Schottel, B.L.; Chifotides, H.T.; Shatruk, M.; Chouai, A.; Pérez, L.M.; Bacsa, J.; Dunbar, K.R. Anion-π Interactions as Controlling Elements in Self-Assembly Reactions of Ag(I) Complexes with π-Acidic Aromatic Rings. *J Am Chem Soc* **2006**, *128*, 5895–5912, doi:10.1021/ja0606273.

87. Aragay, G.; Frontera, A.; Lloveras, V.; Vidal-Gancedo, J.; Ballester, P. Different Nature of the Interactions between Anions and HAT(CN)6: From Reversible Anion−π Complexes to Irreversible Electron-Transfer Processes (HAT(CN)6 = 1,4,5,8,9,12-Hexaazatriphenylene). *J Am Chem Soc* **2013**, *135*, 2620–2627, doi:10.1021/ja309960m.

88. Pancholi, J.; Beer, P.D. Halogen Bonding Motifs for Anion Recognition. *Coord Chem Rev* **2020**, *416*, 213281, doi:https://doi.org/10.1016/j.ccr.2020.213281.

89. Jui, N.T.; Garber, J.A.O.; Finelli, F.G.; MacMillan, D.W.C. Enantioselective Organo-SOMO Cycloadditions: A Catalytic Approach to Complex Pyrrolidines from Olefins and Aldehydes. *J Am Chem Soc* **2012**, *134*, 11400–11403, doi:10.1021/ja305076b.

90. Harding, D.J.; Harding, P.; Phonsri, W. Spin Crossover in Iron(III) Complexes. *Coord Chem Rev* **2016**, *313*, 38–61, doi:10.1016/j.ccr.2016.01.006.

91. Schleyer, P. von R.; Maerker, C.; Dransfeld, A.; Jiao, H.; van Eikema Hommes, N.J.R. Nucleus-Independent Chemical Shifts: A Simple and Efficient Aromaticity Probe. *J Am Chem Soc* **1996**, *118*, 6317–6318, doi:10.1021/ja960582d.

92. Szczepanik, D.W.; Andrzejak, M.; Dominikowska, J.; Pawełek, B.; Krygowski, T.M.; Szatylowicz, H.; Solà, M. The Electron Density of Delocalized Bonds (EDDB) Applied for Quantifying Aromaticity. *Physical Chemistry Chemical Physics* **2017**, *19*, 28970–28981, doi:10.1039/C7CP06114E.

93. Kepler, S.; Zeller, M.; Rosokha, S. V Anion−π Complexes of Halides with P-Benzoquinones: Structures, Thermodynamics, and Criteria of Charge Transfer to Electron Transfer Transition. *J Am Chem Soc* **2019**, *141*, 9338–9348, doi:10.1021/jacs.9b03277.

94. Chifotides, H.T.; Schottel, B.L.; Dunbar, K.R. The π-Accepting Arene HAT(CN)6 as a Halide Receptor through Charge Transfer: Multisite Anion Interactions and Self-Assembly in Solution and the Solid State. *Angewandte Chemie International Edition* **2010**, *49*, 7202–7207, doi:https://doi.org/10.1002/anie.201001755.

95. *CRC Handbook of Chemistry and Physics*; Rumble, J.R., Rumble, J., Eds.; 98th ed.; CRC Press LLC, 2017; ISBN 1498784542.

96. Drougge, L.; Elding, L.I. Mechanisms for Oxidative Addition of Molecular Chlorine to Tetracyanoplatinate(II). Formation of Trans - Dichlorotetracyanoplatinate(IV) via a Platinum(III) Intermediate. *Inorg Chem* **1988**, *27*, 795–798, doi:10.1021/ic00278a011.

97. Mitoraj, M.P.; Michalak, A.; Ziegler, T. A Combined Charge and Energy Decomposition Scheme for Bond Analysis. *J Chem Theory Comput* **2009**, *5*, 962–975, doi:10.1021/ct800503d.

98. Mitoraj, M.; Michalak, A. Natural Orbitals for Chemical Valence as Descriptors of Chemical Bonding in Transition Metal Complexes. *J Mol Model* **2007**, *13*, 347–355, doi:10.1007/s00894-006-0149-4.

99. Chifotides, H.T.; Schottel, B.L.; Dunbar, K.R. The π-Accepting Arene HAT(CN)6 as a Halide Receptor through Charge Transfer: Multisite Anion Interactions and Self-Assembly in Solution and the Solid State. *Angewandte Chemie International Edition* **2010**, *49*, 7202–7207, doi:https://doi.org/10.1002/anie.201001755.

100. Kepler, S.; Zeller, M.; Rosokha, S. V Anion−π Complexes of Halides with P-Benzoquinones: Structures, Thermodynamics, and Criteria of Charge Transfer to Electron Transfer Transition. *J Am Chem Soc* **2019**, *141*, 9338–9348, doi:10.1021/jacs.9b03277.

101. Goerigk, L.; Mehta, N. A Trip to the Density Functional Theory Zoo: Warnings and Recommendations for the User<a Class="reftools" Href="#FN1">*</A>. *Aust J Chem* **2019**, *72*, 563–573.

102. *EPR Spectroscopy: Fundamentals and Methods*; Goldfarb, D., Stoll, S., Eds.; 2018;

103. Clack, D.W.; Hush, N.S.; Woolsey, I.S. Reduction Potentials of Some Metal Phthalocyanines. *Inorganica Chim Acta* **1976**, *19*, 129–132, doi:10.1016/S0020-1693(00)91084-3.

104. Inabe, T.; Tajima, H. Phthalocyanines - Versatile Components of Molecular Conductors. *Chem Rev* **2004**, *104*, 5503–5533, doi:10.1021/cr030649x.

105. Berezin, M.Y.; Achilefu, S. Fluorescence Lifetime Measurements and Biological Imaging. *Chem Rev* **2010**, *110*, 2641–2684, doi:10.1021/cr900343z.

106. Boens, N.; Qin, W.; Basarić, N.; Hofkens, J.; Ameloot, M.; Pouget, J.; Lefèvre, J.P.; Valeur, B.; Gratton, E.; VandeVen, M.; et al. Fluorescence Lifetime Standards for Time and Frequency Domain Fluorescence Spectroscopy. *Anal Chem* **2007**, *79*, 2137–2149, doi:10.1021/ac062160k.